Kinetics of phase ordering in uniaxial and biaxial nematic films

Martin Zapotocky,* Paul M. Goldbart,† and Nigel Goldenfeld‡

Department of Physics and Materials Research Laboratory, University of Illinois at Urbana-Champaign, Urbana, Illinois 61801
(Received 2 May 1994)

The phase ordering process following a quench to both the uniaxial and biaxial nematic phases of a quasi-two-dimensional nematic liquid crystal is investigated numerically. The time dependences of the correlation function, structure factor, energy density, and number densities of topological defects are computed. It is found that the correlation function and the structure factor apparently collapse on to scaling curves over a wide range of times. The correlation length $L_{\mathrm{cor}}(t)$ is found to grow as a power law in the time since the quench t, with a growth exponent of $\phi_{\mathrm{cor}} = 0.407 \pm 0.005$. The growth exponents of the characteristic length scales obtained from the energy length (ϕ_{en}) and the defect number densities (ϕ_{def}), however, are found to differ from ϕ_{cor}. The discrepancy between ϕ_{cor} and ϕ_{def} indicates a violation of dynamical scaling, a violation that is not apparent from our data for the correlation function alone. The observation that all the measured growth exponents are smaller than 0.5 (i.e., the value expected from dimensional analysis) is addressed in terms of properties of point defects in two dimensions, and the annihilation process of an isolated defect pair in a uniaxial nematic phase is investigated. Following the quench to the biaxial nematic phase, there are four topologically distinct defect species present in the system, the populations of which are studied in detail. It is found that only two types of defects are observed in large numbers at late times, and a mechanism for the selection of the prevailing defect species is proposed.

PACS number(s): 64.60.Cn, 61.30.Jf, 82.20.Mj, 05.70.Fh

I. INTRODUCTION

When a system is quenched from a high-temperature equilibrium phase, it undergoes a phase ordering process in which the highly nonequilibrium state, generated during the quench, slowly evolves towards the low-temperature phase. The process of phase ordering following the quench has been extensively studied for systems described by a scalar order parameter [1], and, more recently, also for systems with continuous symmetries. Many of the analytical [2] and numerical [3,4] investigations of the continuous-symmetry cases have concentrated on phase ordering in the $O(N)$-symmetric *vector* model. Very recently, nematic liquid crystals have proven to be useful for experimental investigations of phase ordering [5–7], triggering several theoretical investigations [8–10].

In many experimental and numerical studies it has been observed that *dynamical scaling* holds for the static correlation function at late stages of phase ordering in a variety of systems, some with discrete symmetry [11] and some with continuous symmetry [4,7]. These observations suggest the validity of *the dynamical scaling hypothesis*, according to which there is, at late times t, a single characteristic length scale $L(t)$ that controls the statistical properties of the system. This length can be obtained as the rescaling factor needed to collapse the

correlation function and the structure factor. In systems with topological defects, $L(t)$ is also assumed to determine the average separation of defects. Typically, $L(t)$ is found to obey a power law in time: $L(t) = t^\phi$. All presently available analytical treatments of late stages of phase ordering either *assume* the validity of dynamical scaling (e.g., Ref. [12]), or obtain results consistent with dynamical scaling only after making uncontrolled approximations (e.g., Ref. [13]).

The validity of dynamical scaling, however, has repeatedly been questioned [14,3] for the case of the two-dimensional (2D) $O(2)$ vector model [i.e., the $O(2)$ vector model in two spatial dimensions]. In particular, it has been observed that the correlation length (i.e., the length scale required to cause the collapse of the static correlation function) and the defect separation length appear to grow in time with distinct power laws.

In systems where topologically stable defects exist, many of the universal characteristics of the late stages of phase ordering can be obtained by considering the properties of the defects and their interactions alone. In $O(N)$ vector systems, uniaxial nematic systems and biaxial nematic systems, these properties are distinct from one another [15], and thus one might anticipate differences between the phase ordering of such systems. The study of ordering in systems described by a nematic order parameter is therefore of considerable theoretical interest, and should provide insight into the dependence of the ordering process on the details of order parameter symmetry.

The purpose of this paper is to report results from a cell-dynamical scheme (CDS) simulation of phase ordering in two-dimensional samples of uniaxial and biaxial

---

*Electronic address: zapotock@uiuc.edu
†Electronic address: goldbart@uiuc.edu
‡Electronic address: nigel@uiuc.edu

nematic liquid crystals. By a two-dimensional sample, we mean a film with thickness that is smaller than the equilibrium correlation length prior to the quench. We emphasize that, while the system has two spatial dimensions, the molecules are allowed to point in any direction in three-dimensional space and, correspondingly, the order parameter is a three-dimensional (rank-2 symmetric traceless) tensor. We compute the time dependence of the correlation function, structure factor, energy density, and number densities of the topologically distinct defect species. In common with the 2D O(2) vector model, the system supports point defects, and thus the question of the validity of dynamical scaling is also expected to be relevant here. In the case of a biaxial nematic system, we also study the additional features arising from the fact that the system supports four topologically nonequivalent defect species, and make predictions that should be verifiable experimentally by direct optical visualization of the defects.

This paper is organized as follows. Following the Introduction, we present, in Sec. II, the details of our CDS approach. In Sec. III, we give results for the evolution of the static nematic correlation function, the correlation length, and the energy density, and discuss their implications. In Sec. IV, we review the topological classification of defects in uniaxial and biaxial nematic systems, give algorithms for finding and identifying defects, and illustrate the combination laws among defects using events from our simulation. In Sec. V A, we present results for the time dependence of the density of defects after quenching to the uniaxial nematic phase, and give a detailed discussion of the effective growth exponent for the average defect separation. Defects in biaxial nematic systems have properties qualitatively different from those of uniaxial nematic systems: there are four topologically distinct species of defects, and their combination laws are non-Abelian. In Sec. V B, we present results for the time dependence of the populations of the four topologically stable species, and discuss the physical mechanism that causes certain species to dominate at late times. In Sec. VI, we make some concluding remarks.

We end this Introduction with a summary of our results. We find that the static correlation function and structure factor *appear* to collapse to scaling curves over a wide range of times. In the uniaxial quench case, the correlation length $L_{\text{cor}}(t)$ required to achieve collapse grows approximately as a power law in time, $L_{\text{cor}}(t) \sim t^{\phi_{\text{cor}}}$, with an exponent $\phi_{\text{cor}} = 0.407 \pm 0.005$. The average separation between defects, $L_{\text{def}}(t)$, also grows as a power law, $L_{\text{def}}(t) \sim t^{\phi_{\text{def}}}$, with an exponent $\phi_{\text{def}} = 0.374 \pm 0.007$, distinctly lower than ϕ_{cor}. As we discuss in Sec. V A, the discrepancy between ϕ_{cor} and ϕ_{def} is *inconsistent* with the strict collapse of the correlation function, and thus indicates a violation of dynamical scaling—a violation that is not apparent from our results for the correlation function alone. The length characterizing the decay of the energy density, $L_{\text{en}}(t) \sim t^{\phi_{\text{en}}}$, has the effective growth exponent $\phi_{\text{en}} = 0.320 \pm 0.007$. As we show in Sec. III D, the discrepancy between ϕ_{en} and ϕ_{cor} does not, in fact, indicate the violation of dynamical scaling. The effective growth exponents ϕ_{cor}, ϕ_{def}, and ϕ_{en} are significantly

smaller than the value of 0.5, suggested by naive scaling arguments [16]. A similar reduction of ϕ_{def} has been observed in simulations of the 2D O(2) vector model [3,14]. This has been attributed to logarithmic corrections to the true asymptotic power-law growth of the separation of defects, which was motivated by an analysis of the mutual annihilation of an isolated defect-antidefect pair [17]. In order to check the relevance of the two-defect problem for scaling properties in ordering of large nematic systems, we have performed simulations of the annihilation process of an isolated pair of uniaxial nematic defects. We find that the distance between the defects decays as a power law in the time remaining until annihilation with the growth exponent of 0.375 ± 0.007, consistent with the value of ϕ_{def} given above. The reduced value of the growth exponent in the two-defect problem can be explained by arguments analogous to those used in the treatment of the defect-antidefect annihilation process in Ref. [17].

For the case of biaxial nematic systems, of the four topologically distinct species of defects only two are present in large numbers at late times, giving growth laws with powers of 0.391 ± 0.007 and 0.366 ± 0.007. We characterize the different stages of ordering in the biaxial system in terms of the dominant defect-defect reactions. As in the uniaxial case, we observe a discrepancy between ϕ_{cor} and the growth exponents of the defect separations for each species, indicating a violation of dynamical scaling.

Biaxial nematic media provide perhaps the simplest example of an ordered medium with a non-Abelian fundamental homotopy group [15]. To the best of our knowledge, phase ordering in such systems has not been previously studied. While the physical effects of the non-commutative nature of the fundamental homotopy group are expected to be more profound in three spatial dimensions [18], some consequences are already apparent in the present work.

II. CELL-DYNAMICAL SCHEME FOR THE ENTIRE NEMATIC ORDER PARAMETER

We adopt the standard characterization [19] of the nematic order in the vicinity of the position $\mathbf{r}$ at time t in terms of the order parameter field $Q_{\alpha\beta}(\mathbf{r}, t)$. This order parameter is a traceless symmetric second rank tensor, with Cartesian indices (with $\alpha, \beta, \ldots = 1, 2, 3$). The eigenvalue of $Q_{\alpha\beta}$ largest in absolute magnitude gives the degree of orientation in the preferred direction, the corresponding eigenvector identifying the preferred direction $\mathbf{u}$ (i.e., the so-called director, in the uniaxial nematic case). The difference between the remaining two eigenvalues characterizes the degree of biaxiality, with the biaxiality axis $\mathbf{b}$ specified by the eigenvector corresponding to the second largest eigenvalue [20].

Before the quench, the local value of the order parameter (coarse grained on the scale of the equilibrium correlation length prior to the quench) is zero. After the quench, the eigenvalues of $Q_{\alpha\beta}$ start to grow locally, and the eigenvectors start to become correlated spatially. We

describe the time evolution of the order parameter using the time-dependent Ginzburg-Landau equation appropriate for a nonconserved order parameter:

$$\frac{\partial}{\partial t}Q_{\alpha\beta}(\mathbf{r},t) = -\frac{\delta}{\delta Q_{\alpha\beta}(\mathbf{r},t)}F[Q] \qquad (1)$$

(in which it is understood that only the traceless symmetric part of the right-hand side is retained), where $F[Q] = \int d^2x \mathcal{F}(Q)$ and $\mathcal{F}(Q)$ is the appropriate free energy density.

A homogeneous part of $\mathcal{F}(Q)$ adequate for the description of the isotropic-nematic phase transition can be taken to be [21]

$$\mathcal{F}_h(Q) = A\,\mathrm{Tr}\,Q^2 + B\,\mathrm{Tr}\,Q^3 + C\left(\mathrm{Tr}\,Q^2\right)^2 + E\left(\mathrm{Tr}\,Q^3\right)^2, \qquad (2)$$

with $C > 0$, and the quench corresponds to a change in A, from large and positive in the isotropic phase to negative in the nematic phase. For $E = 0$, Eq. (2) describes a uniaxial nematic system; for $E > 0$, it describes a biaxial nematic system. To construct an effective numerical scheme for the evolution governed by Eq. (1), we use the CDS approach (see below), in which one must find the fixed points of Eq. (1) and Eq. (2) must be ascertained. When diagonalized, $Q_{\alpha\beta}$ can be parametrized (up to a relabeling of axes) as

$$Q = \begin{pmatrix} 2x & 0 & 0 \\ 0 & -x-y & 0 \\ 0 & 0 & -x+y \end{pmatrix}, \qquad (3)$$

with $x \geq 0$ and $0 \leq y < 3x$. (Then $2x$ is the leading eigenvalue if $x < y$, $\frac{3}{2}x$ corresponds to the "degree of ordering" S, as usually defined for uniaxial nematic systems [19], and y characterizes the degree of biaxiality.) The scalar density $\mathcal{F}_h(Q)$ can be expressed as a function of x and y.

Finding and characterizing the stationary points of $\mathcal{F}_h(x,y)$ yields the fixed point diagrams shown in Fig. 1 and Fig. 2. For a uniaxial quench ($E = 0$), one finds

FIG. 2. Fixed-point diagram for the evolution of the order parameter magnitudes x and y following a biaxial quench. The flow is directed towards the stable biaxial fixed point B with the help of the two uniaxial saddle fixed points U and S.

an unstable fixed point at the origin ($x = 0$, $y = 0$), corresponding to the unstable isotropic phase, and a stable fixed point on the uniaxial line $y = 0$, corresponding to the stable uniaxial nematic phase. Furthermore, one finds a saddle fixed point on the line $y = 3x$. The line $y = 3x$ corresponds to a uniaxial phase [two of the eigenvalues in Eq. (3) being equal]; however, the eigenvalue largest in absolute value is $-4x$, and is therefore negative. This indicates "discotic" nematic ordering — for needle-like molecules, it would mean that the long axis of each molecule lies, on average, perpendicular to the "director" (see Fig. 3). Analysis of $\mathcal{F}_h(x,y)$ shows that the fixed point on the $y = 3x$ axis is always present, being stable in the discotic uniaxial direction (along $y = 3x$), and unstable in the biaxial direction (perpendicular to $y = 3x$). The implication of this fixed-point structure is that the time evolution, determined by Eqs. (1) and (2), of the order parameter magnitudes x and y is as schematically indicated in Fig. 1. Similar conclusions were reached in Ref. [10].
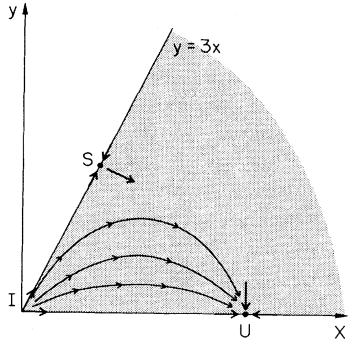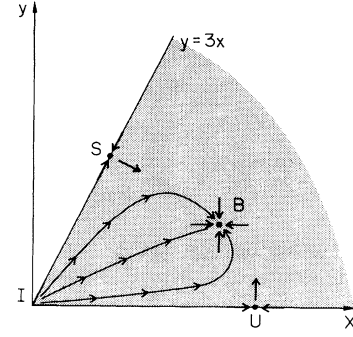

FIG. 1. Fixed-point diagram for the evolution of the order parameter magnitudes x and y following a uniaxial quench. Here I is the unstable fixed point corresponding to the isotropic phase, S is the saddle fixed point on the "discotic" uniaxial axis $y = 3x$, and U is the fixed point corresponding to the stable uniaxial phase.
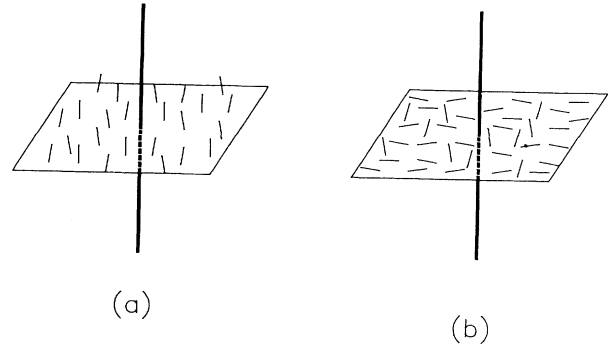
FIG. 3. Two types of uniaxial nematic ordering resulting in the same overall preferred direction of orientation (the director). (a) In needlelike ordering, the long axis of each molecule lies, on average, parallel to the director. (b) In discotic ordering, the long axes of the molecules lie, on average, in the plane perpendicular to the director, with random orientations within the plane.

For the biaxial quench ($E > 0$), the stable fixed point on the uniaxial $y = 0$ axis changes to a saddle fixed point, and redirects the flow towards the stable biaxial fixed point, which is located at $x > 0$ and $0 < y < 3x$ (see Fig. 2). The primary difference between the uniaxial quench and the biaxial quench thus lies in the different structure of the fixed points.

In addition to the homogeneous contribution to the free energy, there is also a contribution that couples the value of the order parameter in different spatial regions. In a nematic system, this elastic energy has three independent contributions, one each from splay, bend, and twist [19]. To simplify calculations, the three corresponding independent elastic constants are commonly taken to be equal (i.e., the so-called one-constant approximation is often made). In this case, the free energy of a nematic phase takes the form

$$\mathcal{F}(Q) = \mathcal{F}_h(Q) + M(\partial_\alpha Q_{\beta\gamma})(\partial_\alpha Q_{\beta\gamma}) , \quad (4)$$

in which $\mathcal{F}_h$ is given by Eq. (2) and M is the (single) elastic constant. The functional derivative $\delta F/\delta Q$ then yields a term $\nabla^2 Q_{\alpha\beta}$ in the equation of motion, Eq. (1), and thus the intercell coupling has a purely diffusive character.

We simulate the dynamics of the order parameter $Q_{\alpha\beta}(\mathbf{r}, t)$ using the CDS technique [11]. The CDS method has proven effective for simulating phase ordering in systems with $O(N)$ vector order parameters (both nonconserved and conserved; see Refs. [3,4]). Recently, ordering of uniaxial nematic systems in two and three spatial dimensions has been studied using CDS techniques [8,9]. In the case of biaxial nematic systems, we encounter a situation in which more than one scalar (i.e., the two independent eigenvalues of the tensor $Q_{\alpha\beta}$) can be constructed from the order parameter (an additional complication is that a linear constraint, $\mathrm{Tr}\, Q = 0$, is imposed on the order parameter components). We shall see below that the CDS approach can be straightforwardly generalized to the present case.

In the CDS approach, the system is divided into cells of the size of the equilibrium correlation length before the quench, and each cell is characterized by a value of the order parameter $Q_{\alpha\beta}$. As we are concerned with a quench from a high temperature, immediately after the quench the values of $Q_{\alpha\beta}$ in each cell are independent (i.e., spatially uncorrelated), identically distributed random variables. Each time step of the evolution of the $Q_{\alpha\beta}$ field is divided into two substeps: single-cell evolution, and intercell coupling.

In the single-cell evolution step, which reflects the homogeneous contribution to the free energy, we must assign a new value Q_{new} to the order parameter in a given cell as a function of the old value in that cell Q_{old}. By using symmetry arguments one can show that the most general symmetric traceless function Q_{new} of a symmetric traceless tensor Q_{old} can be written as

$$Q_{\mathrm{new}} = f\left(\mathrm{Tr}\, Q_{\mathrm{old}}^2, \mathrm{Tr}\, Q_{\mathrm{old}}^3\right) Q_{\mathrm{old}}$$
$$+ g\left(\mathrm{Tr}\, Q_{\mathrm{old}}^2, \mathrm{Tr}\, Q_{\mathrm{old}}^3\right) Q_{\mathrm{old}}^2\Big|_{dt} , \quad (5)$$

where f and g are arbitrary (scalar) functions of the two independent scalars $\mathrm{Tr}\, Q_{\mathrm{old}}^2$ and $\mathrm{Tr}\, Q_{\mathrm{old}}^3$, and $Q^2|_{dt} \equiv Q^2 - \frac{1}{3}\mathbb{1}\,\mathrm{Tr}\, Q^2$ (where $\mathbb{1}$ is the unit matrix) is the traceless part of Q^2.

The choice of the functions f and g is motivated by the form of the homogeneous free energy, Eq. (2). As the asymptotic dynamics of the order parameter is governed by the fixed-point structure of Eqs. (1) and (2), we are free to choose f and g in any (computationally efficient) way, as long as the map, Eq. (5), has the fixed-point structure of Fig. 1 or Fig. 2. (One can pass from the independent scalars $\mathrm{Tr}\, Q^2$ and $\mathrm{Tr}\, Q^3$ to x and y, as defined above, by using the identities

$$x = \sqrt{\tfrac{1}{6}\mathrm{Tr}\, Q^2} \cos\left\{\tfrac{1}{3}\arccos[\sqrt{6}\mathrm{Tr}\, Q^3/(\mathrm{Tr}\, Q^2)^{3/2}]\right\} \text{ and}$$

$$y = \sqrt{\tfrac{1}{2}\mathrm{Tr}\, Q^2 - 3x^2}.)$$ The numerical results in the remainder of this paper have been obtained using the choice

$$f(x, y) = 1.3\tanh(x)/x - x\, g(x, y), \quad (6a)$$
$$g(x, y) = 1/4 \quad (6b)$$

in the case of a uniaxial quench, and

$$f(x, y) = 1.3\tanh(x)/x - x\, g(x, y), \quad (7a)$$
$$g(x, y) = -1/4 + b\, y \quad (7b)$$

in the case of the biaxial quench. The parameter b controls the strength of biaxiality. It is straightforward to check that the choices reflected in Eqs. (6) and (7) give the fixed-point structure of Fig. 1 and Fig. 2, respectively, with fixed-point locations (x, y) at $(0, 0)$, $(0.977, 0)$, $(0.337, 1.011)$ (in the biaxial case, the location of the third fixed point depends on the parameter b), and (for the biaxial quench only) at $(0.977, 1/4b)$. The results presented in the remainder of this paper were obtained using the choice $b = 1$, with the exception of the data in Fig. 6(b), where the value $b = 0.5$ was used.

Note that Eqs. (3) and (5) imply that $x' = x[f(x, y) + xg(x, y)] - \frac{1}{3}y^2 g(x, y)$, where x and y are calculated from Q_{old}, and x' is calculated from Q_{new}. Our choices of f and g (for both the uniaxial [Eqs. (6)] and biaxial [Eqs. (7)] quench) therefore ensure that $x' = 1.3\tanh(x)$ for $y = 0$—that is, the evolution of the degree x of uniaxial ordering is (in the absence of biaxiality) given by the standard CDS choice (see, e.g., Ref. [11]) for the evolution of the order parameter magnitude. We find Eqs. (6b) and (7b) to be the simplest computationally efficient choices for $g(x, y)$ ensuring the correct properties of the flow in the biaxiality-strength (y) direction.

The intercell coupling contribution to the CDS evolution resulting from the elastic contribution to the free energy in Eq. (4) can be expressed as

$$Q_{\mathrm{new}} = Q_{\mathrm{old}} + D\left(Q_{\mathrm{old}} - \langle\langle Q\rangle\rangle\right). \quad (8)$$

Here, Q_{new} is the value of Q in a certain cell after the update, D is a parameter reflecting the elastic coupling, and the term $\langle\langle Q\rangle\rangle$, defined by

$$\langle\langle Q \rangle\rangle \equiv \frac{1}{6}\sum_{NN} Q + \frac{1}{12}\sum_{NNN} Q , \qquad (9)$$

arises from a discretization of the Laplacian that retains nearest (NN) and next nearest (NNN) neighbor terms [11].

The quenches that we are considering are envisaged to start at high temperatures, at which the equilibrium phase is the disordered, isotropic phase. We take as the initial condition for our CDS simulation a configuration representative of this phase, in which Q is zero in each cell, apart from small, uncorrelated, isotropically distributed, random fluctuations. Specifically, the random initial order parameter in each cell was obtained by generating three random numbers that add to zero (i.e., three eigenvalues of Q) from a uniform distribution of width 0.2, and then rotating the resulting diagonal matrix using random Euler angles. To summarize the scheme, we start with a random initial configuration (satisfying periodic boundary conditions), and then repeatedly apply the steps specified in Eqs. (5) and (8), using the appropriate map, i.e., Eq. (6) or (7).

The results presented in the remainder of this paper were obtained in runs using a variety of choices of the diffusion constant D (in the range $D = 0.1$–0.5). Higher values of D were found to be more advantageous for accessing the asymptotic regime in a given number of time steps. It was, however, necessary to use lower values of D in the detailed investigation of the evolution of the populations of the topological defects because, at the early stages of ordering, values of $D \simeq 0.5$ lead to the presence of a number of cells where the eigenvalue largest in absolute value is negative (that is, the corresponding points in Figs. 1 and 2 lie above the line $y = x$), which invalidates the notion of a topologically stable defect (see Sec. IV A). We found that by "hardening" the random initial configuration (i.e., allowing it to evolve for a small number of time steps with D set to zero, so that the order parameter magnitudes x and y approach the fixed point without affecting the *orientation* of the order parameter), and subsequently using the value $D = 0.1$ to evolve the system, we were able both to ensure that the topological defects are well defined even at the earliest stages of ordering and to access the asymptotic late time regime.

We are concerned with quenches to zero temperature, so that thermal fluctuations play no role in the dynamics. It was, however, commonly observed in previous numerical investigations of zero-temperature quenches that freezing into metastable configurations can occur (e.g., Ref. [17]). Therefore, to test whether freezing effects were influencing our simulation, we performed a limited number of runs in the presence of *noise* (i.e., a small-amplitude random configuration was added to the order parameter at each time step). The results were observed to be insensitive to noise, up to noise strengths capable of spontaneously generating numerous defect pairs. All results in the asymptotic regime were observed to be independent of the chosen value of D and the system size (with the exception of the transition in the rate of change

of the effective growth exponents, mentioned in the following section).

III. CORRELATION FUNCTION, STRUCTURE FACTOR, AND ENERGY DENSITY

A. Collapse of the correlation function and the structure factor

In its usual formulation, the dynamical scaling hypothesis [1,12] states that at late times of phase ordering there is a single time-dependent characteristic length scale $L(t)$ that controls the statistical properties of the system. Stated another way, the system is statistically self-similar at successive times, up to a rescaling determined by $L(t)$. It will be crucial in the detailed analysis of the data from our simulation to distinguish two statements which are often taken to be consequences of dynamical scaling.

(a) The correlation function $C(\mathbf{r}, t)$ at different times t can be collapsed on to a single curve by using the characteristic length scale $L_{cor}(t)$:

$$C(\mathbf{r}, t) = \Gamma(r/L_{cor}(t)) \qquad (10)$$

where $\Gamma(y)$ is a scaling function.

(b) The length scale $L_{cor}(t)$ used to obtain the collapse of the correlation function determines the characteristic length scale of all time-dependent macroscopic quantities in the system. Thus the energy density of the system as well as the number density of point defects present decay as $L_{cor}(t)^{-d}$, where d is the spatial dimensionality of the system.

We shall see in our simulations of the 2D nematic system that statement (a) is apparently very well satisfied over a wide range of times, but that statement (b) is rather strongly violated. A detailed discussion of whether this indicates a breakdown of dynamical scaling will be given in Secs. III D and V A.

The characteristic length scale $L_{cor}(t)$ is usually assumed to grow asymptotically as a power law of time, $L_{cor}(t) \sim t^{\phi_{cor}}$ for t large. It should be noted that such an assumption does not, in principle, follow from the dynamical scaling hypothesis. The length scales investigated in our simulation grow as approximate power laws at late times. However, the growth exponents for these length scales differ and, moreover, are significantly lower than the value $\phi_{cor} = 0.5$, which is usually observed in experiments on phase ordering in systems with nonconserved order parameters. The latter issue is discussed in detail in Sec. V A.

We now present the results for the correlation function and the structure factor from our simulation. For the tensorial nematic order parameter $Q_{\alpha\beta}(\mathbf{r}, t)$, a scalar correlation function can be defined by

$$C(r, t) = \frac{\left\langle \text{Tr}\left[Q(\mathbf{0}, t)\, Q(\mathbf{r}, t)\right] \right\rangle}{\left\langle \text{Tr}\, Q(\mathbf{0}, t)^2 \right\rangle}, \qquad (11)$$

where $\langle \cdots \rangle$ denotes averaging over the positions (i.e., $\mathbf{0}$), and over the orientations of $\mathbf{r}$. The correlation function is normalized so that $C(0,t) = 1$. We define the correlation length $L_{\mathrm{cor}}(t)$ at time t through

$$C(r,t)\Big|_{r=L_{\mathrm{cor}}(t)} = 1/2 \,. \qquad (12)$$

Figure 4 shows the correlation functions $C(r,t)$ obtained from our simulation of ordering in a biaxial system at a sequence of times. In Fig. 5, data from Fig. 4 are rescaled using the correlation length defined by Eq. (12). We see that a good collapse of the correlation function is obtained in the range of times $200 < t < 5000$. A collapse of similar quality is also obtained for the correlation function in the uniaxial system. We have, in addition, calculated the structure factor $S(k,t)$ [i.e., the spatial Fourier transform of $C(r,t)$], and used the correlation length defined by Eq. (12) to check the validity of the scaling form

$$S(k,t) = L_{\mathrm{cor}}^2(t)g\Big(kL_{\mathrm{cor}}(t)\Big) \,. \qquad (13)$$

The resulting scaling functions $g\big(kL_{\mathrm{cor}}(t)\big)$ for the uniaxial and biaxial quenches are plotted in Figs. 6(a) and 6(b). [The "tail" of $g(y)$, i.e., the asymptotic behavior of $g(y)$ in the $y \gg 1$ region, will be discussed in more detail in Sec. III D.] The quality of the collapse of our data for both the correlation function and the structure factor is entirely comparable to the quality of collapse obtained in simulations of ordering in systems where the validity of dynamical scaling has not been questioned (see, e.g., Ref. [11] for the Ising system in two spatial dimensions, or Ref. [14] for the $O(3)$ vector model in three dimensions). In this sense, our data are consistent with the validity of the statement (a), given above.

FIG. 5. Collapse of the data for $C(r,t)$ from Fig. 3. Inset: time dependence of the correlation length L_{cor}, defined by $C(r,t)|_{r=L_{\mathrm{cor}}(t)} = 1/2$.

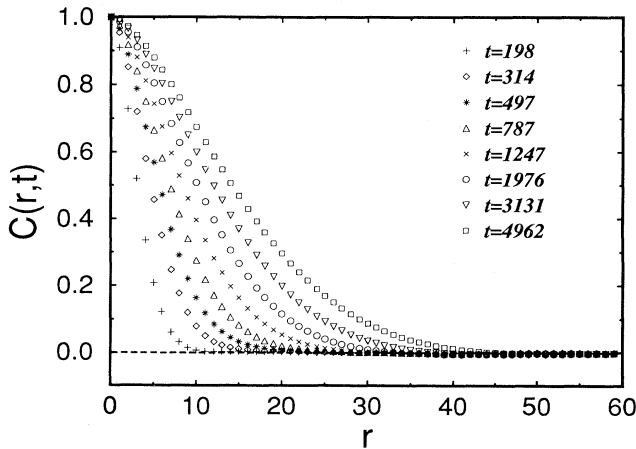

FIG. 4. Correlation function $C(r,t)$ at specified values of time t following the biaxial quench. The data were obtained by averaging over 68 configurations of a 256×256 system, with diffusion constant $D = 0.1$.
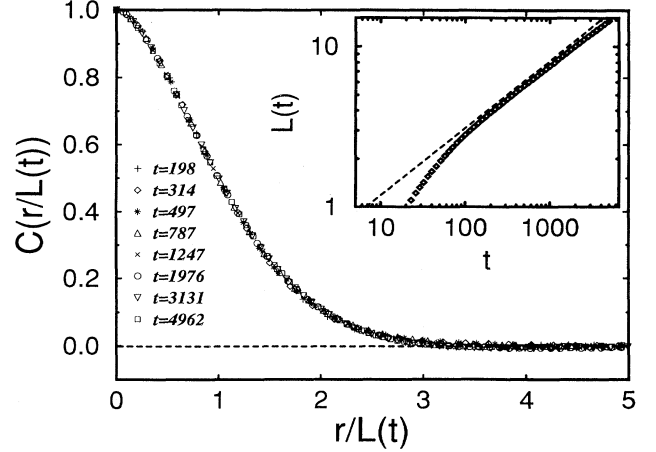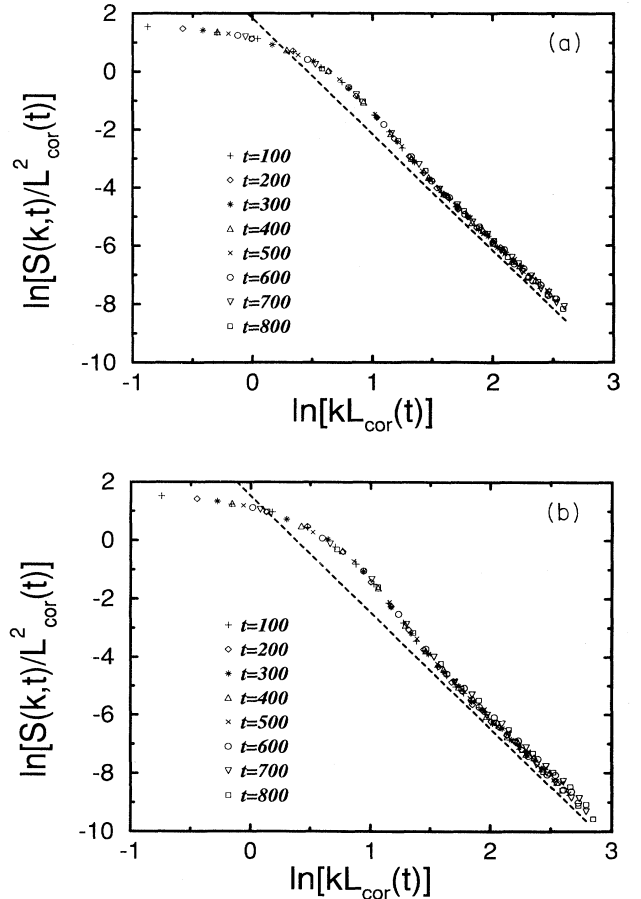
FIG. 6. The collapsed structure factor scaling function $g(kL_{\mathrm{cor}}) = S(k,t)/L_{\mathrm{cor}}^2(t)$ for (a) uniaxial and (b) biaxial quenches. In both cases, the average was performed over 100 configurations of a 100×100 system, with the diffusion constant $D = 0.1$. A straight line with slope -4 is plotted in both (a) and (b) to demonstrate the validity of the Porod law, $g(y) \sim y^{-4}$ for y large (see Sec. III C).

B. Effective growth exponents for the correlation length and energy length

We now consider the time dependence of the correlation length and the energy density. The inset in Fig. 5 shows the growth of the correlation length $L_{cor}(t)$. This log-log plot indicates a crossover from a non-power-law growth of $L_{cor}(t)$ at small t to an approximate power-law growth at $t \geq 200$, the later range of times corresponding to times where the good collapse of the correlation function is observed. The slope of the best-fitting straight line, giving the growth exponent, is $\phi_{cor} = 0.41$. In Fig. 7, we plot the elastic free energy of the system, $\int (\partial_\alpha Q_{\beta\gamma})(\partial_\alpha Q_{\beta\gamma}) d^2x$, as a function of time. Asymptotically, the elastic free energy decays approximately as $t^{-0.64}$, giving power-law growth for the energy length scale $L_{en}(t)$ (defined as the inverse square root of the elastic free energy) with exponent $\phi_{en} = 0.32$.

To determine the value of the growth exponent for both cases in a more reliable way, we calculate the *effective growth exponent* $\hat{\phi}(t)$, defined as

$$\hat{\phi}(t) \equiv \frac{d \ln L(t)}{d \ln(t)} , \qquad (14)$$

in the considered time range [with $L(t)$ taken to be either $L_{cor}(t)$ or $L_{en}(t)$]. The true (asymptotic) power-law exponent ϕ is obtained by extrapolating the effective exponent $\hat{\phi}(t)$ to very large values of t or, equivalently, to very large values of $L(t)$. We have attempted to match our data for $\hat{\phi}(t)$ on to two candidate extrapolation formulas:

$$\hat{\phi}(t) = \phi + \frac{a}{L(t)} , \qquad (15a)$$

$$\hat{\phi}(t) = \phi + \frac{A}{t} , \qquad (15b)$$

FIG. 8. Effective growth exponents for the correlation length (upper curve) and the energy length (lower curve) in the biaxial quench case, plotted to fit the extrapolation formula (15b).

with ϕ, a, and A constant. The validity of relation (15a) would imply that

$$L(t) = -\frac{a}{\phi} + bt^\phi \qquad (16a)$$

throughout the considered time range, while the relation (15b) would imply that

$$L(t) = c t^\phi \exp\left(- A/t \right) \qquad (16b)$$

(where b and c are arbitrary constants).

We find that our data for the effective growth exponents of both the correlation length and the energy length fit Eq. (15b) significantly better than Eq. (15a) (see Figs. 8 and 9). As $t \gg 1$ in the considered time range, we can rewrite Eq. (16b) as

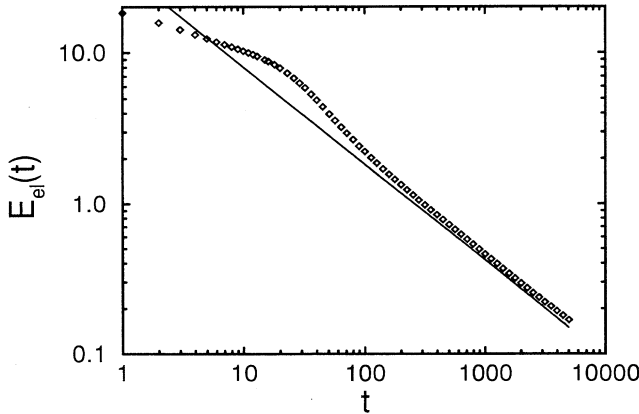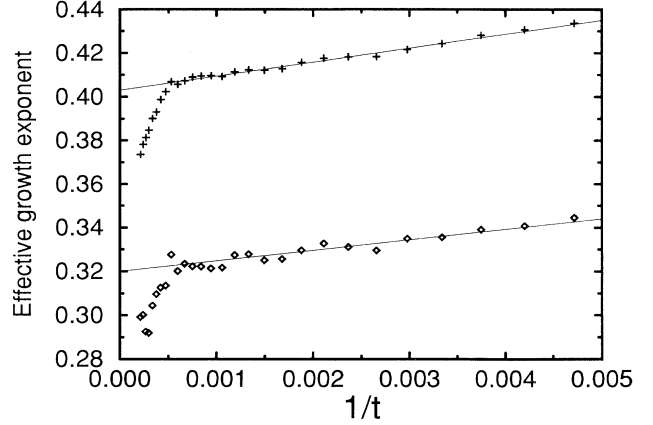$$L(t) \approx c t^\phi \left(1 - \frac{A}{t}\right) = c t^\phi - cAt^{\phi-1} , \qquad (17)$$

FIG. 7. Log-log plot of the elastic free energy per cell $E_{el}(t)$ versus time t (averaged over 68 configurations of a 256×256 system).
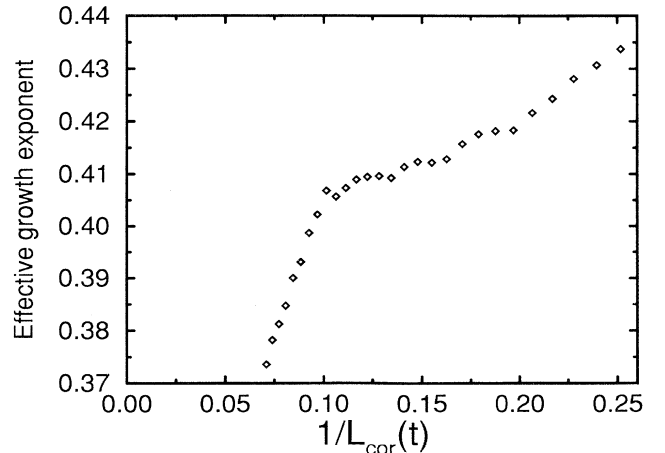

FIG. 9. Effective growth exponent $\hat{\phi}_{cor}(t)$ for the correlation length in the biaxial case, plotted to fit the extrapolation formula (15a).

which (by analogy with critical phenomena having a "critical point" at $t = \infty$) corresponds to a power-law behavior together with the leading *analytic correction*. The extrapolation formula (15b) is thus perhaps more natural than (15a).

The effective exponents $\hat{\phi}_{cor}(t)$ and $\hat{\phi}_{en}(t)$ are plotted as a function of $1/t$ in Fig. 8 (for the biaxial quench case) and in Fig. 10 (for the uniaxial quench case). The figures show a sharp transition in the rate of change of both effective exponents at the time $t \simeq 2000$. (The transition is less sharp in the uniaxial quench data, because the average was performed over a smaller number of configurations than for the biaxial case.) We found that in a system of smaller size, i.e., 100×100, a similar transition occurred at a lower value of t [and therefore $L(t)$], indicating a connection between this transition and finite-size effects. At the same time, increasing the diffusion constant D in the CDS to values larger than $D = 0.1$ seemed partially to suppress the transition, indicating that the rapid lowering of the growth exponents may be due to the onset of freezing. (The likelihood of freezing at late times was observed to depend on the value of the diffusion constant in CDS simulations for scalar systems [11].) To determine the asymptotic growth exponents we therefore used data only from the time range $200 < t < 2000$.

In the biaxial quench case, the extrapolation formula (15b) yields (see Fig. 8) the asymptotic exponent values $\phi_{cor} = 0.403 \pm 0.003$ for the correlation length and $\phi_{en} = 0.320 \pm 0.005$ for the energy length. A similar analysis for the uniaxial quench (see Fig. 10) gives $\phi_{cor} = 0.407 \pm 0.005$ and $\phi_{en} = 0.325 \pm 0.007$, consistent with the biaxial values. Statement (b) in Sec. III A (i.e., the presence of a *single* characteristic length scale) is therefore violated in the considered time range. We are thus confronted with two questions: (i) why is ϕ_{en} significantly lower than ϕ_{cor}; and (ii) why are both ϕ_{cor} and ϕ_{en} different from the value 0.5, suggested by the diffusive character of the equation of motion (1) and by scaling arguments [16]? The second question can be most naturally addressed by

investigating in detail the process of annihilation of a pair of defects, as will be discussed in Sec. V A. The first question is addressed below. First, however, we need to discuss in some detail the form of the structure factor scaling function $g(y)$.

C. The "tail" of the structure factor

We see in Figs. 6(a) and 6(b) that the function $g(y)$, obtained by collapsing the structure factor using the correlation length [see Eq. (13)], decays asymptotically as y^{-4} at large y. This is readily understood by generalizing the arguments leading to the "Porod law tail," i.e., $g(y) \sim y^{-(N+d)}$ in the case of the $O(N)$ vector model in d dimensions [22,23]. For $y = kL_{cor}(t) \gg 1$, the structure factor $S(k,t)$ probes the order parameter configurations at length scale $1/k = L_{cor}(t)/y$ much smaller than the separation between defects, which is of the order of $L_{cor}(t)$ (see the note [24]). Substantial variations of the order parameter over a length scale of $L_{cor}(t)/y$ occur only in the vicinity of the defect cores, and are not related to interdefect correlations. It is therefore possible to calculate the value of $S(k,t)$ for $kL(t) \gg 1$ from the order parameter configuration close to the core of an isolated defect. This implies that

$$S(k,t) = \rho_{def}(t)\, u(k) \qquad [\text{for } kL_{cor}(t) \gg 1]\,, \qquad (18)$$

where ρ_{def} is the density of defects in the system and $u(k)$ is a function of k only. Let us assume for now [25] that the separation between defects scales as the correlation length $L_{cor}(t)$, so that $\rho_{def} \propto L_{cor}(t)^{-(d-s)}$, where s is the dimensionality of the defect. Then the validity of the scaling form (13) implies that

$$g(y) = Ay^{-[d+(d-s)]}\,, \qquad (19)$$

i.e., the scaling function $g(y)$ decays asymptotically as a power law, with the exponent given by the sum of the dimension of space d and the *codimension* of the defect $(d - s)$. In the case of the d-dimensional $O(N)$ vector model, the dimensionality of the defects is $s = d - N$, and we recover the result $g(y) \propto y^{-(d+N)}$ of [22,23]. In our 2D nematic system, which has point defects, the codimension is $2 - 0 = 2$, yielding $g(y) \sim y^{-4}$, in agreement with the results of our simulations [see Figs. 6(a) and 6(b)].

It is of interest to note that at lower values of y [i.e., values less than $y = kL_{cor}(t) \simeq 5$], the scaling functions in Figs. 6 deviate from the y^{-4} law, seeming instead to decay with a *higher* power of y. Similar behavior was observed in simulations [8] and experiments [7] (see also Ref. [10]) of phase ordering in *three-dimensional* uniaxial nematic systems, where a final Porod law decay exponent of 5 (corresponding to *line* defects in three dimensions) was approached *from above*. It was speculated that the transient value higher than 5 was due to the influence of point defects (which in three dimensions give a Porod law exponent of 6); in our *two-dimensional* simulation, however, no defects (even transient) that would contribute
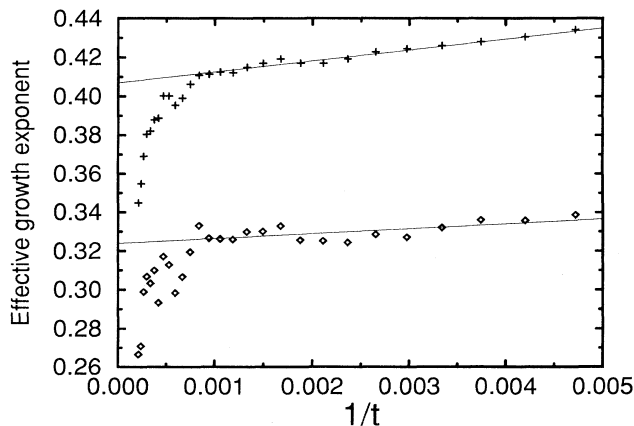

FIG. 10. Effective growth exponents for the correlation length (upper curve) and energy length (lower curve) in the uniaxial quench case, plotted to fit the extrapolation formula (15b). The system size is 256×256, and averaging was performed over 35 configurations.

a Porod law exponent higher than 4 occur, and it must therefore be concluded that the faster decay of $g(y)$ at intermediate values of y is associated with interdefect correlations. This is further indicated by the fact that deviations from the asymptotic Porod law start to occur at values of $y \simeq 5$ (see Figs. 6), corresponding to correlations probed on the scale of $\frac{2\pi}{y} L_{\text{cor}}(t) \simeq L_{\text{cor}}(t)$, i.e., the order of the interdefect distance.

D. The energy length growth exponent

We are now in a position to discuss why it is that the growth exponent ϕ_{en} was found to be significantly lower than ϕ_{cor} in our numerical results. To do this, we derive a formula relating the instantaneous exponents $\hat{\phi}_{\text{en}}(t)$ and $\hat{\phi}_{\text{cor}}(t)$. A similar argument was given in a qualitative form for the O(2) vector order parameter case in Ref. [23].

We start by noting that

$$E_{\text{el}} = \int d^2x (\partial_\alpha Q_{\beta\gamma})(\partial_\alpha Q_{\beta\gamma})$$

$$= \int d^2k \, k^2 S(k,t)$$

$$= \int d^2k \, [kL_{\text{cor}}(t)]^2 g(kL_{\text{cor}}(t)) , \qquad (20)$$

where we used statement (a) of the scaling hypothesis in the form of Eq. (13). Next, we use the Porod law form, Eq. (19), for $g(y)$ in the range of distances $L_{\text{cor}}(t) \geq r \geq \xi$, where ξ is the core size of the defects. (The contribution to the integral in Eq. (20) from the range of distances $\infty > r > L_{\text{cor}}(t)$ scales as $[L_{\text{cor}}(t)]^{-2}$, and is subdominant for large $L_{\text{cor}}(t)$.) By integrating Eq. (20) from ξ to $L(t)$, we obtain the asymptotic [large $L_{\text{cor}}(t)$] expression for the free energy

$$E_{\text{el}} \propto L_{\text{cor}}(t)^{-2} \ln[L_{\text{cor}}(t)/\xi] . \qquad (21)$$
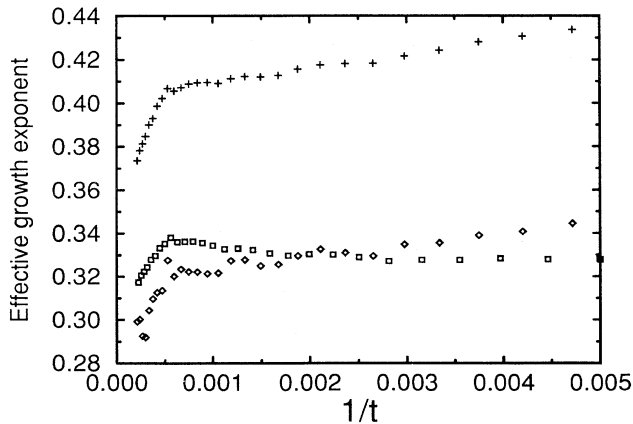
This implies that

FIG. 11. Comparison of the measured values of the energy length growth exponent $\hat{\phi}_{\text{en}}(t)$ (shown as ◇) to the values predicted by formula (23) (shown as □); the measured values of the correlation length growth exponent $\hat{\phi}_{\text{cor}}(t)$, used in formula (23), are shown as crosses (+, upper curve).

$$\frac{d(\ln E_{\text{el}})}{d(\ln t)} = \frac{d[\ln L_{\text{cor}}(t)]}{d(\ln t)} \frac{d(\ln E_{\text{el}})}{d(\ln L_{\text{cor}})}$$

$$= \hat{\phi}_{\text{cor}}(t)\left(-2 + \frac{1}{\ln(L_{\text{cor}}/\xi)}\right) . \qquad (22)$$

Therefore, the effective growth exponent $\hat{\phi}_{\text{en}}(t)$ for the characteristic energy length is depressed with respect to the correlation length exponent $\hat{\phi}_{\text{cor}}(t)$, according to

$$\hat{\phi}_{\text{en}}(t) \simeq \hat{\phi}_{\text{cor}}(t) - \frac{\hat{\phi}_{\text{cor}}(t)}{2\ln[L_{\text{cor}}(t)/\xi]} . \qquad (23)$$

In Fig. 11 we compare the prediction of Eq. (23) to the measured value (see Fig. 4) of the effective exponent $\hat{\phi}_{\text{en}}(t)$, for the plausible value of the core size $\xi = 0.5$ lattice spacings (direct inspection of the order parameter magnitudes in the vicinity of defect locations in our simulation shows that the core size is less than, but of the order of, one lattice spacing). Considering the crudeness of the argument leading to (23), the agreement of Eq. (23) with our data is quite satisfactory.

IV. PROPERTIES OF TOPOLOGICAL DEFECTS IN UNIAXIAL AND BIAXIAL NEMATIC SYSTEMS

A. Topological classification of nematic defects

Certain features of the late stages of phase ordering may be understood in terms of the properties of topological defects present in the system [26]: the exponent and amplitude of the asymptotic power-law decay of the structure factor can be calculated from the configuration of the order parameter around a single defect [22]; in systems for which dynamical scaling holds, the time-dependent characteristic length scale is given by the separation of defects; and logarithmic corrections to power-law scaling of the average defect separation can be attributed to the form of the interdefect forces [17]. It is therefore important to understand in detail the properties of topological defects in the system at hand. In this subsection, we review the main consequences of the classification of topologically stable defects in uniaxial and biaxial nematic systems [15]. In Sec. IV C we illustrate these consequences with data from our simulation. The time evolution of the number densities of defects during phase ordering in our system will be analyzed in detail in Sec. V.

For the unambiguous topological classification of order parameter configuration, it is necessary that the invariants constructed from the order parameter avoid certain values. In the O(N) vector model, this amounts to avoiding zeros in the magnitude of the vector. In the context of the nematic order parameter, it is furthermore necessary that the order parameter magnitudes x and y (defined in Sec. II) are restricted to lie either in the region $x > y$ [needlelike ordering, Fig. 3(a)] or in the region $x < y$ [discotic ordering, Fig. 3(b)]. In order to develop the topological classification, it is sufficient to impose the condition that throughout the system the values of the order pa-

rameter magnitudes x and y are appropriate constants. What remain are orientational degrees of freedom, two for the uniaxial case (as specified by a three-dimensional "headless"unit vector, i.e., the director) and three for the biaxial case. In our simulations, we ensure the applicability of the topological classification, even at the earliest stages after the quench, as discussed at the end of Sec. II.

We first discuss defects in the uniaxial nematic systems. Consider the order parameter configuration in a 2D system in which the director rotates by 360° around a central point [Fig. 12(a)]. Such a configuration is singular (in the sense that the free energy density diverges at its center), but it is not *topologically stable*: by continuously rotating the director out of the plane (i.e., by "escaping into the third dimension") we can arrive at the nonsingular (i.e., finite free energy density) configuration, as shown in Fig. 12(b). The singular configuration in Fig. 13 (in which the director rotates by 180°) is, however, topologically stable: in the process of attempting to escape into the third dimension, an even more singular configuration with a (semi-)infinite line defect would be generated. More generally, any configuration in which the director rotates by an even multiple of 180° can be continuously deformed into the trivial configuration, shown in Fig. 12(b), in contrast with configurations having a rotation of an odd multiple of 180°, which can be deformed into the configuration in Fig. 13. Note, in particular, that configurations with rotations of +180° (clockwise) and −180° (counterclockwise) can be deformed into each other. Thus, for the 2D uniaxial nematic system there exists only one class of topologically stable point defects, exemplified by the order parameter configuration shown
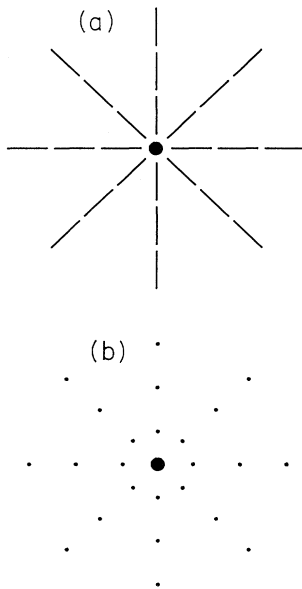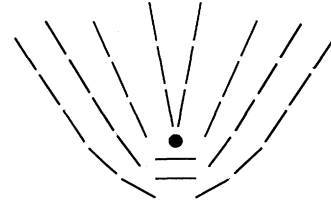

FIG. 13. A configuration of the director corresponding to the 180° defect in a uniaxial nematic phase. An attempt to escape from such a configuration by rotating the director at each location out of the page inevitably results in a singular line extending from the defect center to infinity, separating regions where the director rotates out of the page in opposing directions.

in Fig. 13. (This class contains all defects obtainable by continuous distortions, including those in which the director is rotated out of the plane.)

The combination law for two stable defects is also readily obtained: colliding two ±180° configurations results in a configuration with either 360° or 0° rotation, both of which are topologically trivial. Therefore any two stable defects can mutually annihilate upon colliding. In more formal language, the properties discussed above are a consequence of the fact that the first homotopy group of the uniaxial nematic order parameter space is the two-element group $Z_2 = [\{0,1\}$ under addition modulo 2]. The elements 0 and 1 correspond to the topologically trivial class of configurations and to the stable defect class, respectively. The defects combine according to a law given by the group operation $1 + 1 = 0$.

Next, we discuss defects in *biaxial* nematic systems, for which the situation is more complicated. Here, the first homotopy group of the order parameter space Π_1 (giving the classification of point defects in a 2D system) is the non-Abelian eight-element group of quaternions, which can be represented as

$$\Pi_1 = \{1, -1, i\sigma_x, -i\sigma_x, i\sigma_y, -i\sigma_y, i\sigma_z, -i\sigma_z\}, \quad (24)$$

where σ_k are the Pauli matrices, and the group operation corresponds to matrix multiplication. For a non-Abelian Π_1, the classes of topologically nonequivalent defects are given by the *conjugacy classes* of Π_1 (see, e.g., [15] for a detailed discussion). The quaternion group Eq. (24) has five conjugacy classes:

$$C_0 = \{1\}, \quad (25a)$$
$$\overline{C}_0 = \{-1\}, \quad (25b)$$
$$C_x = \{i\sigma_x, -i\sigma_x\}, \quad (25c)$$
$$C_y = \{i\sigma_y, -i\sigma_y\}, \quad (25d)$$
$$C_z = \{i\sigma_z, -i\sigma_z\}. \quad (25e)$$

FIG. 12. (a) A configuration of the director corresponding to the 360° defect in a uniaxial nematic phase. (b) By rotating the director at each location out of the page, one can smoothly deform the configuration in (a) to the defect-free configuration in (b), with the director everywhere perpendicular to the page.

Thus there is a topologically trivial defect class (C_0), and four nontrivial defect classes ($\overline{C}_0, C_x, C_y, C_z$). These are characterized by the winding numbers of the uniaxial axis $\mathbf{u}$ and the biaxial axis $\mathbf{b}$ of the order parameter tensor: in $\overline{C}_0$ defects, either $\mathbf{u}$ or $\mathbf{b}$ (or both) rotate by 360°; in C_x defects, $\mathbf{u}$ rotates by ±180° and $\mathbf{b}$ does not rotate;

TABLE I. Combination laws for the four distinct classes (C_x, C_y, C_z, and $\overline{C}_0$) of pointlike topological defects in a two-dimensional biaxial nematic system. C_0 represents a topologically trivial configuration; $C_0 + \overline{C}_0$ indicates that the resulting configuration can be either in class C_0 or in $\overline{C}_0$ (we omit the multiplicities of classes). Table taken from Ref. [15].

	C_0	$\overline{C}_0$	C_x	C_y	C_z
C_0	C_0	$\overline{C}_0$	C_x	C_y	C_z
$\overline{C}_0$	$\overline{C}_0$	C_0	C_x	C_y	C_z
C_x	C_x	C_x	$C_0 + \overline{C}_0$	C_z	C_y
C_y	C_y	C_y	C_z	$C_0 + \overline{C}_0$	C_x
C_z	C_z	C_z	C_y	C_x	$C_0 + \overline{C}_0$

in C_y defects, $\mathbf{u}$ does not rotate and $\mathbf{b}$ rotates by $\pm 180°$; and in C_z defects, both $\mathbf{u}$ and $\mathbf{b}$ rotate by $\pm 180°$.

The group operation laws of the quaternion group, Eq. (24), imply multiplication laws for its classes, as summarized in Table I. These give the combination laws for the four nontrivial defect types: thus, combining a C_y defect and a C_z defect yields a C_x defect, while combining a C_y defect with $\overline{C}_0$ results in a configuration that remains in the C_y class. Two C_y defects can either mutually annihilate or combine to give a $\overline{C}_0$ defect; the result depends on the details of the order parameter configuration, in particular, on the winding of the path of approach of the two C_y defects among other defects present in the system. (This complication is a consequence of the noncommutative nature of our homotopy group Π_1 [27].)

The validity of the results of the topological classification presented above was directly confirmed experimentally in three spatial dimensions by De'Neve et al. [28]. In 3D, the fundamental homotopy group, Eq. (24), classifies line defects. In Ref. [28], four inequivalent types of disclination, corresponding to the four nontrivial conjugacy classes in Eq. (25), were observed experimentally in a biaxial nematic system; their combination laws were found to be in agreement with those in Table I. We are not aware of any published experimental work on defects in effectively two-dimensional biaxial nematic systems.

B. Defect-finding algorithms

To keep track of the evolution of the large populations of defects present during phase ordering (and to distinguish the four species of defect in biaxial nematic systems), an effective defect-finding algorithm based on the topological properties of the defects is needed. Before illustrating the defect properties discussed above (as we do in Sec. IV C), we present the defect-finding algorithms used in our simulation. This can also serve to illuminate further the topological classification scheme. The present subsection may be skipped by the reader interested primarily in the results without impairing the understanding of the remainder of the paper.

Consider first the case of the uniaxial nematic system. The order parameter coset space is a sphere with antipodal points identified (reflecting the inversion symmetry of the director), i.e., the projective plane RP_2. If we

trace a loop around the center of any topologically unstable singular configuration [e.g., as in Fig. 12(a)], we generate a *contractible* loop in the order parameter space [Fig. 14(a)]. In the case of a topologically stable configuration (e.g., Fig. 13), we generate a *noncontractible* loop in the projective plane [Fig. 14(b)], connecting two antipodal points on the sphere. Thus we arrive at the following algorithm for deciding whether a (uniaxial) stable defect is located inside the region spanned by the cells with coordinates (x, y), $(x+1, y)$, $(x+1, y+1)$, $(x, y+1)$: we find the uniaxial direction in the cell (x, y) and choose as our starting point one of its intersections with the order parameter sphere (Fig. 15). The uniaxial direction in the cell $(x + 1, y)$ has two intersections with the order parameter sphere; we choose the point that is *closer* to the starting point as the next point of the loop in the order parameter space. This amounts to assuming that the new uniaxial direction was reached by rotating through the smallest possible angle, so as to minimize the cost in free energy. We continue with the cells $(x + 1, y + 1)$ and $(x, y + 1)$, again choosing the point on the order parameter sphere closer to the previous point. We close the path by again looking at the two intersection points in the cell (x, y): if the original starting point is closer to the point assigned to the cell $(x, y + 1)$ then we classify the configuration as not topologically stable; if the antipodal point is closer then we classify the configuration as having a stable defect located at the intersection of the cell boundaries. In a previous work on phase order-
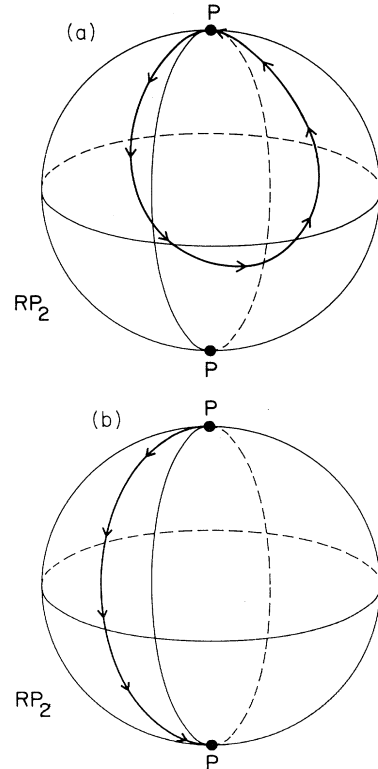

FIG. 14. Contractible (a) and noncontractible (b) loops connecting two identical points (P and P') in the uniaxial nematic order parameter space RP_2.
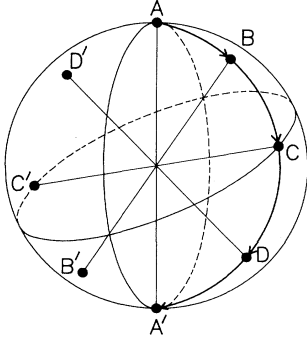
FIG. 15. The algorithm for finding defects in a uniaxial nematic (see Sec. IV B for details). The diameters AA', BB', CC', and DD' correspond to the uniaxial directions of the order parameter in cells (x, y), $(x + 1, y)$, $(x + 1, y + 1)$, and $(x, y + 1)$, respectively.
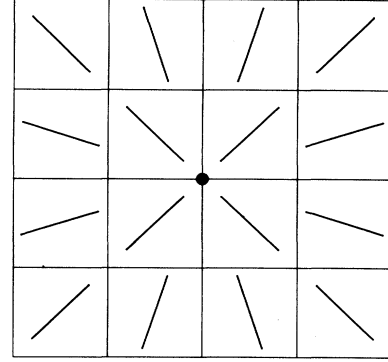

FIG. 16. A typical configuration of the uniaxial or biaxial direction of the order parameter in the 4×4 array with a $\overline{C}_0$ defect in the center. Notice that no C_x, C_y, or C_z defects are present in the array.

ing in uniaxial nematic systems [9], vortices were sought by considering whether the total angle of rotation of the uniaxial direction projected on to one of the three perpendicular planes was 180°. For a configuration in which the director in all cells lies in one plane, as in the case of an isolated defect (as in Fig. 12), the two algorithms are equivalent; for other configurations, however, the "projection" algorithm can be unreliable. We find that our "topological" algorithm can consistently identify all defects, even when the interdefect separation is of the order of one lattice spacing.

For biaxial nematic systems, we can distinguish the three 180° defect classes by applying the uniaxial algorithm twice, once to the uniaxial direction **u** and once to the biaxial direction **b**: e.g., the C_y defect will give a **u** loop that returns to the starting point and a **b** loop that ends at the antipodal point. The 360° defect (class $\overline{C}_0$) cannot be found using this algorithm. This is a consequence of the fact that the biaxial nematic order parameter coset space is not simply a direct product of two projective planes. Thus, for this case, we use the "projection" algorithm on a 4×4 array of cells: if the total rotation of the projection (on at least *two* planes) of two of the **u**, **b**, and **u** × **b** directions in the 12 boundary cells is ±360°, *and* if no 180° defects are found inside the 4×4 array, then we identify the center of the array as a $\overline{C}_0$ defect (see Fig. 16). Note that to consider a 2×2 array would be inadequate because the total rotation in a 4-cell path is, by definition, at most 180°; a 3×3 array cannot be used, because the 360° rotation is in that case tied to the existence of two 180° defects inside the array. The algorithm that we use for finding the $\overline{C}_0$ defect is thus less robust than that which we use for finding the other defect types. As we shall see in the next section, however, the $\overline{C}_0$ defect is present at late times only in very small numbers, and its influence is not important for our primary conclusions.

C. Results illustrating the topological classification scheme

We now illustrate the properties of defects in uniaxial and biaxial nematic systems that we discussed in

Sec. IV A using results from our simulation. Defects in nematic films can be observed experimentally via birefringence patterns in light transmitted through films situated between crossed polarizers (i.e., Schlieren patterns). The intensity of transmitted light is minimal when the projection of the director on to the polarization plane is parallel to the transmission axis of either polarizer; the 180° (360°) defects are therefore identified as intersections of two (four) dark brushes in the transmitted pattern [19]. In Figs. 17(a)–17(c), we show the Schlieren patterns obtained for configurations generated in our simulations at a sequence of times after a uniaxial quench [29]. As these figures show, the process of ordering occurs through the mutual annihilation of the numerous 180° defects.

In Figs. 18(a)–18(e), we exhibit the locations of defects, found using the defect-finding algorithms discussed above, in a typical sequence of configurations following a biaxial quench in a small system. Defects from each of the four topologically stable classes are present in the system. The observed two-defect events confirm the topological combination laws given in Table I (as described in the captions to Figs. 18). Occasionally, "many-defect" events, where a number of neighboring defects interact in a way not uniquely separable into two-defect events, are observed; the frequency of these events can be decreased by reducing the diffusion constant in the CDS map to values below $D = 0.1$.

It can be seen from Table I that the *defect number parities* p_1, p_2, and p_3, defined by

$$p_1 = (n_x + n_y) \bmod 2 , \tag{26a}$$

$$p_2 = (n_y + n_z) \bmod 2 , \tag{26b}$$

$$p_3 = (n_x + n_z) \bmod 2 , \tag{26c}$$

are conserved during all reactions among defects. Here n_x, n_y, and n_z respectively denote the number of defects from classes C_x, C_y, and C_z; as $(p_1 + p_2 + p_3) \bmod 2 = 0$, only two of the three parities are independent. In our simulations the parities, Eqs. (26), were observed to be conserved in all reactions, regardless of the number of

TABLE II. Numbers of defects in the C_x, C_y, C_z, and $\overline{C}_0$ classes at time t after the quench to the biaxial nematic phase in a 256×256 system (the value of $D = 0.1$ was used in the simulation).

t	$n(C_x)$	$n(C_y)$	$n(C_z)$	$n(\overline{C}_0)^a$
0	14925	11503	15039	0
5	10093	12787	14577	1
10	6393	12949	12141	5
20	2758	10542	8866	13
40	589	6157	5357	14
100	25	2495	2359	24
200	1	1439	1235	9
399	2	840	676	3
795	0	514	394	7
1585	0	326	244	5
2819	2	200	146	1
5012	0	130	116	6

[a]The number of $\overline{C}_0$ defects which can be found at early times is reduced due to the high density of the 180° defects—see Sec. IV C.

participating defects. In addition, the parities obtained from the *total* numbers of defects present in the whole system must be *even*, as we have adopted periodic boundary conditions. The reason for this is that opposite edges of the boundary of the system map on to iden-tical (closed) curves in the order parameter coset space, but are traversed in opposite senses; the loop consisting of the boundary of the system therefore maps into a contractible loop in the coset space. Thus the configuration of the system, as a whole, is topologically trivial, which for the nematic system implies that the parities, Eqs. (26), are even. This property of the global parities is confirmed in Table II, which gives the numbers of C_x, C_y, and C_z defects found during a typical run in a system of size 256×256.

V. EVOLUTION OF THE DEFECT POPULATIONS

In this section, we present results for the time evolution of the total number of defects in each of the topologically inequivalent defect classes.

A. Results for the uniaxial quench; growth law for the separation between defects

In uniaxial nematic systems there is only one class of stable defects. In Fig. 19 we show the number of such defects as a function of time since the uniaxial quench, in a system of size 256×256, averaged over

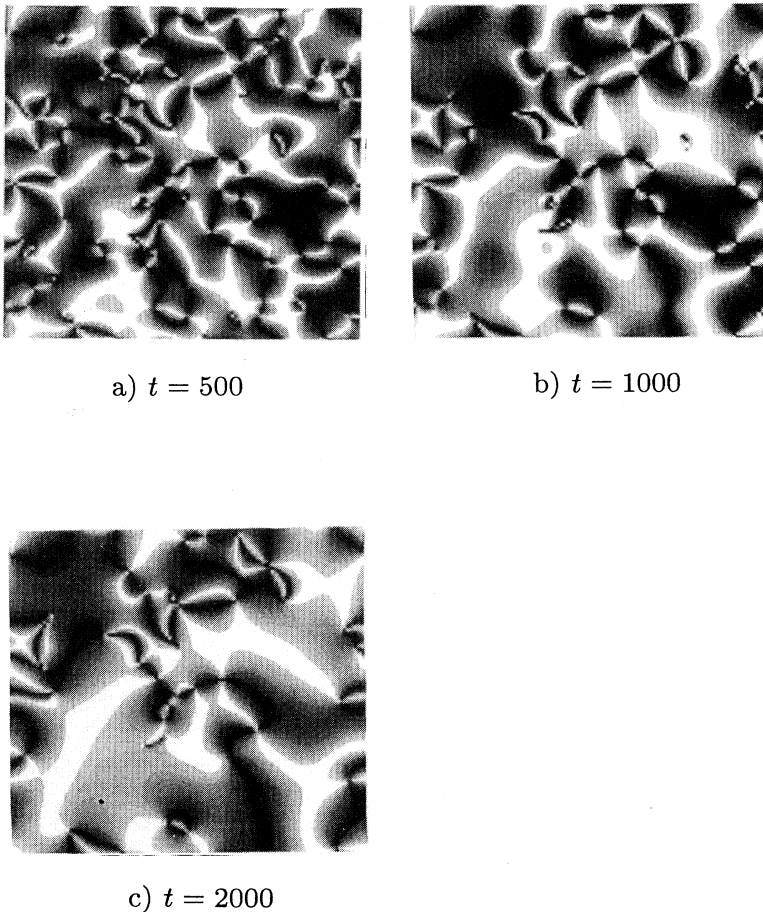

a) $t = 500$ b) $t = 1000$

c) $t = 2000$

FIG. 17. Intensity of light transmitted through a uniaxial nematic film situated between crossed polarizers (the Schlieren pattern). We show a system of size 100×100 at times $t = 500$, $t = 1000$, and $t = 2000$ after the quench. The defects appear in the pictures as the intersections of two bright and two dark lines.

35 sets of initial configurations. In the inset we plot the effective growth exponent $\phi_{\mathrm{def}}(t)$ for the average interdefect distance $L_{\mathrm{def}}(t)$ versus $1/t$, in the interval where the correlation function collapses. The intercept with the $\hat{\phi}_{\mathrm{def}}$ axis gives the asymptotic growth exponent

$\phi_{\mathrm{def}} = 0.374 \pm 0.005$ [see formula (15b) and the discussion in Sec. III B]. The growth exponent obtained from the number of defects differs from the exponents obtained from the correlation function and the energy density (see Sec. III A), giving another indication of the violation of

a) $t = 17$

b) $t = 18$

c) $t = 44$

d) $t = 45$

e) $t = 46$
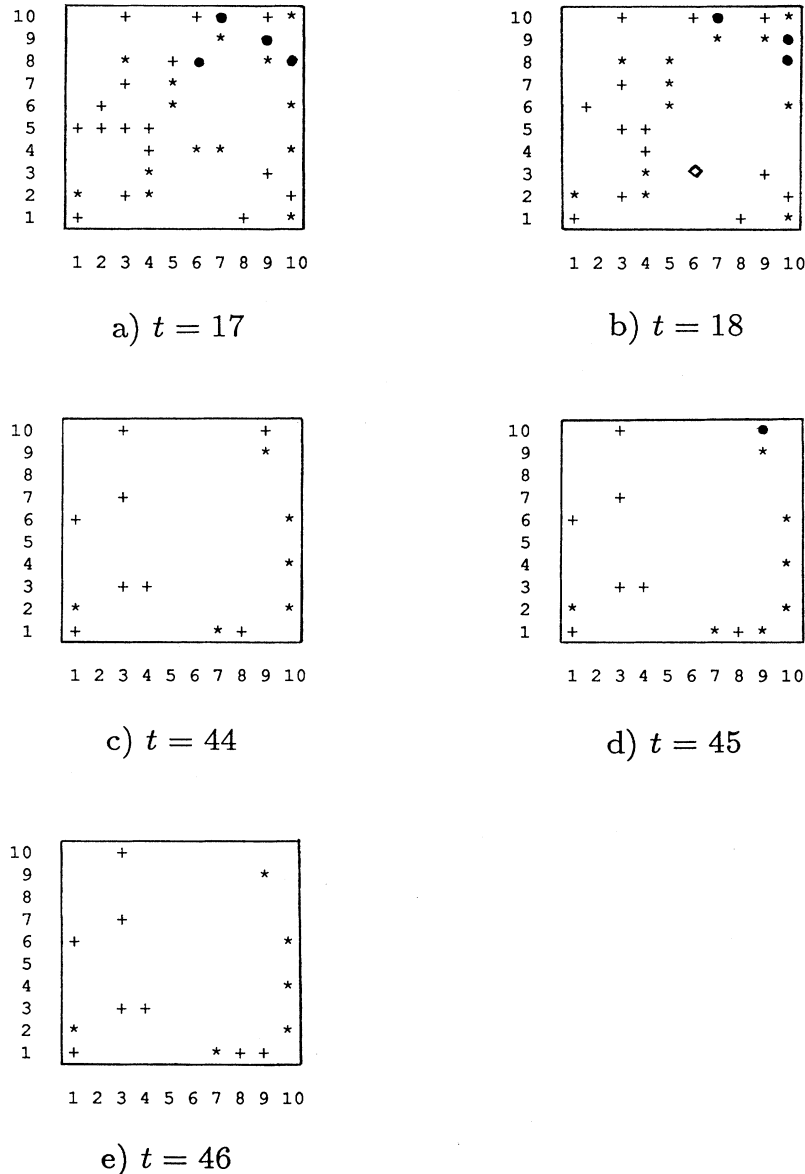
FIG. 18. Defect configurations in a biaxial system of size 10×10 at specified times since the quench. The symbols $\bullet$, $*$, $+$, and $\diamond$ correspond to defects from classes C_x, C_y, C_z, and $\overline{C}_0$, respectively. In the following description of the figures, we refer to the horizontal coordinate as x, and to the vertical coordinate as y, both starting from the left bottom corner of each figure (thus $x,y = 1, ..., 10$). Note that the boundary conditions are periodic. The diffusion constant value of $D = 0.1$ was used in this simulation. (a) The configuration at $t=17$ time steps since the quench. The system contains four type C_x defects, 16 type C_y defects, and 14 type C_z defects. (b) The configuration at the next time step ($t=18$). The C_z defect at $(x,y) = (1,5)$ annihilated with the neighboring C_z defect. Two C_y defects in the center region combined to produce a $\overline{C}_0$ defect. The C_z defect at $(x,y) = (5,8)$ and the C_x defect at $(x,y) = (6,8)$ combined to a C_y defect. (c) The configuration at $t=44$. All the C_x defects have decayed from the system. (d) At the next time step ($t=45$), the C_z defect at $(x,y) = (9,10)$ disintegrates into the C_x defect and the C_y defect at the neighboring site $(x,y) = (9,1)$. (e) Configuration at the next time step ($t=46$). The C_x defect immediately recombines with the C_y defect at $(x,y) = (9,1)$. The net result of the last two reactions is a C_x-mediated jump of the C_z defect from the site $(x,y) = (9,10)$ to the neighboring site $(x,y) = (9,1)$. The C_z defect at $(x,y) = (9,1)$ undergoes annihilation with the C_z defect at $(x,y) = (8,1)$ at a later time.
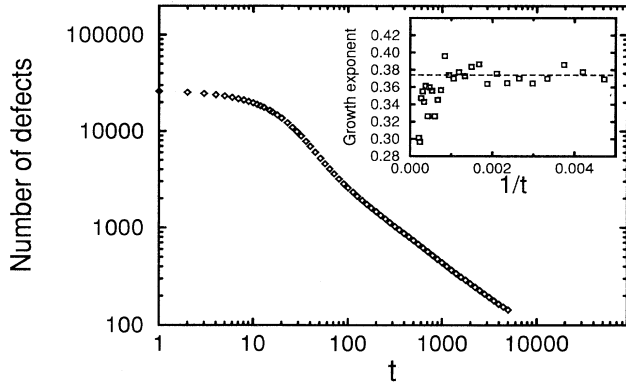
FIG. 19. Log-log plot of the number of defects in a uniaxial system (size 256 × 256, averaged over 35 configurations) as a function of time t since the quench. Inset: the effective growth exponent $\hat{\phi}_{def}(t)$ of the average separation between the defects, plotted to fit the extrapolation formula (15b).

statement (b) of the dynamical scaling hypothesis, at least over the range of times studied.

It has been found in all published numerical studies of phase ordering in 2D systems with point defects (e.g., Refs. [3,8,9,14]) that both the correlation length and (where studied) the separation of defects grow *more slowly* than the $t^{1/2}$ power growth law that is suggested by dimensional analysis [16]. This issue was addressed theoretically for the O(2) vector model in Ref. [17], by starting from the equation of motion for an isolated defect-antidefect pair, which follows from equating the attractive and frictional forces acting on each defect. The elastic attractive force was taken to be $F_{at} \propto -1/\mathcal{D}$, where $\mathcal{D}$ is the separation of the defect pair. The frictional force was taken to be $F_{fr} \propto v \ln(R/\xi)$, where R is the size of a defect, ξ is the size of its core, and $v = \frac{1}{2}\frac{d\mathcal{D}}{dt}$ is its velocity. For an isolated defect-antidefect pair, $R \sim \mathcal{D}$. By equating F_{at} and F_{fr} Yurke et al. obtained an implicit formula for the dependence of the separation $\mathcal{D}$ on the time remaining before annihilation τ:

$$\mathcal{D}(\tau) = \text{const} \times \left[\frac{\tau}{\ln\left[\mathcal{D}(\tau)/\xi\right] - 1/2} \right]^{1/2}. \quad (27)$$

Yurke et al. then argued that the same expressions for the elastic and frictional forces acting in an isolated defect-antidefect pair may be used in a modification of the arguments in Ref. [16] to obtain an expression, identical to Eq. (27), for the growth of the average separation between defects in a system undergoing phase ordering. In this scenario, τ is (up to an undetermined, but small, additive constant) the time elapsed since the quench, and $\mathcal{D}$ is the average separation of defects, L_{def}, so that one obtains

$$L_{def}(t) = \text{const} \times \left[\frac{t}{\ln\left[L_{def}(t)/\xi\right] - 1/2} \right]^{1/2}. \quad (28)$$

Equation (28) implies that L_{def} grows asymptotically

as $t^{1/2}$, but that the effective growth exponent $\hat{\phi}_{def} = d \ln L_{def}/d \ln t$ approaches the value 1/2 only slowly and from below, due to the logarithmic term. It was indeed observed in the numerical simulations reported in Ref. [17] that, both for the annihilation of an isolated defect-antidefect pair and for phase ordering of a large system after a quench, $\hat{\phi}_{def}(t)$ was significantly smaller than 1/2, and tended to increase with increasing separation of defects.

It is important to recall that in the system investigated in our simulations—namely, the 2D (uniaxial) nematic system—the director can point in any direction in the three-dimensional space, in contrast to the restriction on the order parameter of the 2D O(2) vector model to lie in the plane. The late time features of phase ordering, however, are governed primarily by the point defects moving in two-dimensional space, which are present in both models. For this reason, it is appropriate to compare our results to the conclusions of Ref. [17]. (We note, parenthetically, that the 2D O(3) vector model does not support any topologically stable singular configurations, and its phase ordering exhibits features [30] strongly different from the phase ordering in the 2D nematic system.)

Equation (28) implies that the effective growth exponent for the average defect separation is given by

$$\frac{d \ln L_{def}(t)}{d \ln t} = \frac{t}{L_{def}(t)^2} \frac{\text{const}}{2 \ln[L_{def}(t)/\xi]}. \quad (29)$$

Due to the unknown constant in Eq. (29), it is not possible (even with the knowledge of the core size, $\xi \simeq 0.5$ lattice spacings, from Sec. III) to compare the numerical value of the effective growth exponent $\phi_{def} \simeq 0.374$ in our simulation to the expression (29). Although Eq. (28) predicts an increasing effective exponent $\phi_{def}(t)$, the value obtained from our data is essentially constant over the interval during which collapse of the correlation function occurs (Fig. 19).

A crucial assumption made in deriving Eq. (28) is that the average separation of the numerous defects during the phase ordering of a large system is determined solely by the forces acting in the two-defect problem. In order to address the validity of this assumption, we simulated the annihilation process of two isolated uniaxial nematic defects (see Fig. 20). During this simulation, we found it advantageous (in order to be able to reduce the influence of the discrete character of the lattice by averaging over multiple runs) to add a random order parameter configuration of reduced amplitude (up to 10% of the full order parameter magnitude) at each time step. We stress that this noise was added solely to obtain a meaningful averaging procedure; no pinning effects were observed in the studied time range upon eliminating the noise. The measured distance between the two defects $\mathcal{D}$ is shown in Fig. 21 as a function of time remaining to annihilation, t. The power law $\mathcal{D} \propto t^{0.375}$ is observed over the range of distances $2 \leq \mathcal{D} \leq 10$, corresponding to the range in which the effective exponent $\phi_{def} \simeq 0.375$ was observed in the phase ordering simulation (Fig. 19). We therefore reach the conclusion that the time dependence of the distance between two isolated annihilating defects does in-
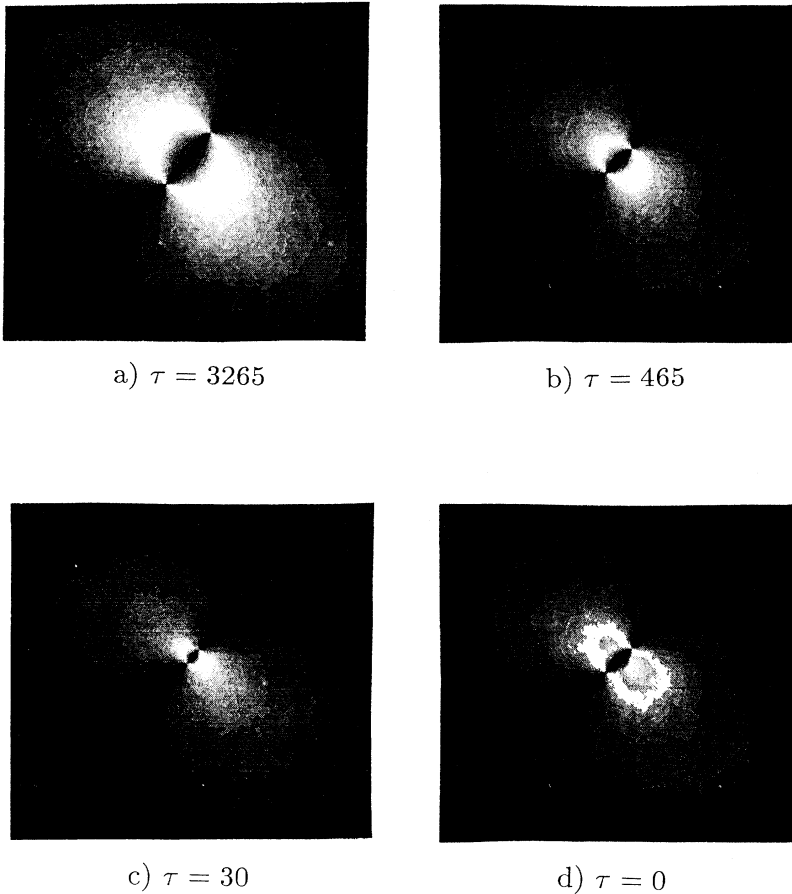
a) $\tau = 3265$ b) $\tau = 465$

FIG. 20. Schlieren patterns showing two approaching uniaxial defects at times $t=3265$, $t=465$, and $t=30$ before annihilation, and one time step after annihilation. The system size was 100×100; the value of the diffusion constant was $D = 0.3$; weak noise (10% of the order parameter magnitude) was added at each time step.

c) $\tau = 30$ d) $\tau = 0$

deed determine the growth rate of the average separation between defects during phase ordering.

Around an isolated pair of uniaxial nematic defects, it is energetically advantageous for the director to lie in a single plane. The treatment of the annihilation process of two defects is then identical to the treatment for the 2D XY model case in Ref. [17] [with the constant in Eq. (27) divided by 4, due to the change in the winding number of the defects]. Our data (Fig. 21) do not, however, show the increase of the effective exponent $\phi_{\mathrm{def}}(t)$, with increasing $\mathcal{D}$, predicted by Eq. (27). This increase should be visible even in the comparatively narrow range of $\mathcal{D}$ covered in our simulation. This we take as an indication that the forces acting on the defects in our simulation are not completely described by the forces $F_{\mathrm{fr}} \propto v \ln(\mathcal{D}/\xi)$ and $F_{\mathrm{at}} \propto 1/\mathcal{D}$, assumed in the derivation of (27). In particular, the influence of a weak pinning potential at the centers of the cells would become more pronounced with increasing $\mathcal{D}$, since the interaction energy of two vortices decreases with increasing distance. The presence of a pinning force would therefore tend to decrease the effective growth exponent ϕ_{def} with increasing $\mathcal{D}$, possibly offsetting the increase of ϕ_{def} predicted by Eq. (27).

It should be noted that the arguments leading to Eq. (29) do not make any assumptions about the correlation function—in particular, our finding that the correlation length (as defined in Sec. III A) and the aver-

age separation of defects scale in a different way ($\phi_{\mathrm{cor}} = 0.407 \pm 0.005$ versus $\phi_{\mathrm{def}} = 0.374 \pm 0.007$) does not invalidate Eq. (29).

We now discuss the implications of the observed inequality $\phi_{\mathrm{cor}} > \phi_{\mathrm{def}}$. This inequality is, strictly speaking,
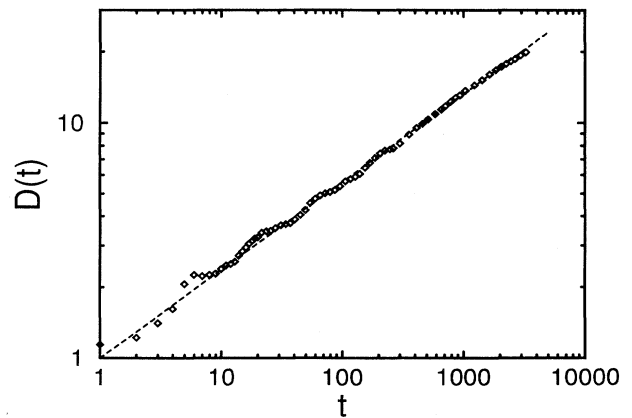

FIG. 21. The distance $\mathcal{D}(t)$ between two annihilating uniaxial defects as a function of time t remaining till annihilation. A weak value of noise (10% of the order parameter magnitude) was used to permit averaging over 20 events. The value of the diffusion constant was $D = 0.3$.

incompatible with the collapse of the correlation function and structure factor [i.e., statement (a) in Sec. III A]. The reason is that the *number density of defects* ρ_{def} appears in Porod's law, Eq. (18), which is valid independently of the collapse of the structure factor. The density ρ_{def} must decay as the (square of the) separation between defects (and not any other length, such as L_{cor}). In order that Eq. (13), expressing the collapse of the structure factor, be compatible with Eq. (18) it is therefore necessary that the lengths L_{cor} and L_{def} have a common time dependence. We have not been able to identify why L_{cor} and L_{def} differ. However, it is plausible that the origin of the discrepancy lies in the relevance of additional degrees of freedom beyond the defect positions.

Recall that earlier, in Sec. III, we exhibited the good collapse of the correlation function and structure factor in our simulation. It is thus seen that the direct comparison of the effective growth exponents ϕ_{def} and ϕ_{cor} presents a more sensitive diagnostic of the validity of dynamical scaling than do the apparent collapse of the correlation function and structure factor.

We remind the reader that the discrepancy between ϕ_{cor} and the energy length growth exponent ϕ_{en} does *not* necessarily indicate the breakdown of dynamical scaling, as we have explained in Sec. III. On the other hand, the expression for the difference between ϕ_{cor} and ϕ_{en}, Eq. (23), was derived in Sec. III D under the assumption that the structure factor collapses. Given the quality of the apparent collapse and the smallness of the difference between ϕ_{cor} and ϕ_{def} we anticipate only small corrections to Eq. (23).

The discrepancy between the growth exponents of the correlation length and of the defect separation was recently observed (Ref. [14]) also in the two-dimensional O(2) vector model. It is interesting to note that the results obtained in Ref. [14], $\phi_{\mathrm{cor}} = 0.42$ and $\phi_{\mathrm{def}} = 0.37$, are numerically very close to the results obtained by us in the nematic order parameter case.

B. Results for the biaxial quench; selection of the prevailing defect species

In the biaxial nematic case, we monitor separately the populations of the four inequivalent defect classes in-
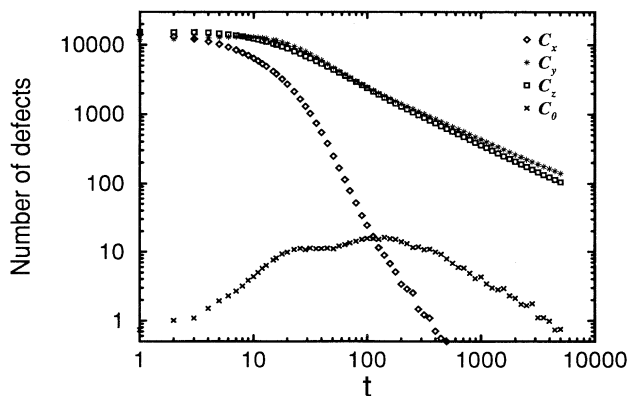

FIG. 22. Log-log plot of the numbers of the C_x, C_y, C_z, and $\overline{C}_0$ defects as a function of time since the biaxial quench (averaged over 68 configurations of a 256 × 256 system).
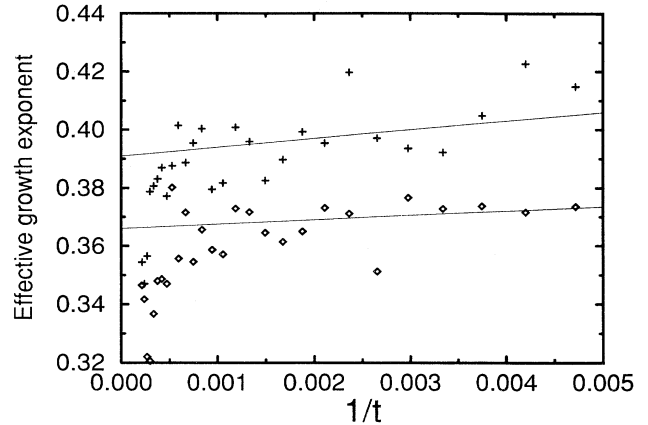

FIG. 23. Effective growth exponents for the separation between C_y defects (shown as ◊) and between C_z defects (shown as +), analyzed using the extrapolation formula (15b).

troduced in Sec. IV. Figure 22 shows the results averaged over 68 initial configurations of a 256 × 256 system. Immediately following the quench, defects from the classes C_x, C_y, and C_z are present in large numbers. We find that the C_x defect population decays rapidly in the initial stages of ordering, and disappears from the system at the time approximately corresponding to the onset of the regime in which there is apparent collapse of the correlation function. The C_y and C_z defects subsequently remain in the system in roughly equal numbers, and determine the properties of the asymptotic regime. The effective growth exponent for the C_y and C_z defect separation is analyzed in Fig. 23 using the method described in Sec. III A; we obtain $\phi_{\mathrm{def}} = 0.366 \pm 0.005$ and $\phi_{\mathrm{def}} = 0.391 \pm 0.005$, respectively.

The evolution of the $\overline{C}_0$ (i.e., 360°) defect population requires further clarification. Our defect-finding algorithm (see Sec. IV B) is able to identify a $\overline{C}_0$ defect within any given 4 × 4 array of cells only if there are no 180° defects within the array; at the initial stages of ordering, however, very few such arrays exist in the system, due to the high density of C_x, C_y, and C_z defects. Accordingly, the detected number of $\overline{C}_0$ is very small at early times after the quench (see Fig. 22), and becomes a reliable measure of the proportion of 360° defects in a real system only at late times, when the separation between 180° defects is much larger than the lattice spacing. A more meaningful quantity, perhaps, is the ratio of the number of $\overline{C}_0$ defects to the number of the "available" 4 × 4 arrays; this ratio is plotted in Fig. 24. The population of $\overline{C}_0$ defects appears to decay slightly faster than both the C_y and C_z defect populations at the late times; note, however, that our statistics for the $\overline{C}_0$ defects are rather poor.

We now suggest an explanation of the observed rapid decay of the C_x population, and the presence, in comparable numbers, of the C_y and C_z defects in the late time regime. According to Table I, a pair of C_x, C_y, or C_z defects can annihilate to give a topologically trivial configuration. These processes indeed occur frequently in
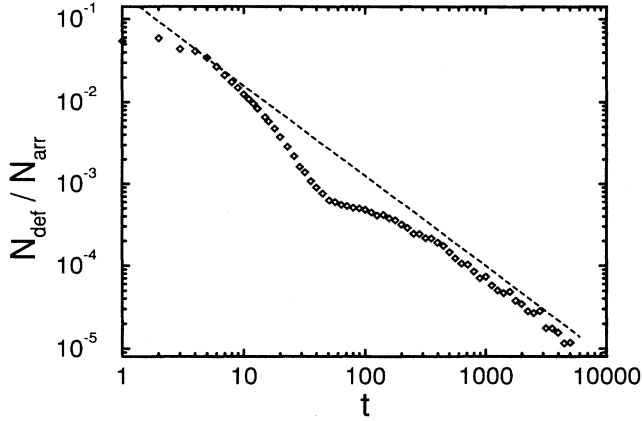
FIG. 24. The ratio of the number of $\overline{C}_0$ defects to the number of 4×4 arrays of cells with no $180°$ defects, plotted as a function of time. The slope of the straight line is -1.10.

the simulation (see Fig. 18). After the system takes advantage of these "decay channels," however, two nearby defects of the same species are frequently "screened" by a defect of a different species located between them. The system can then reduce the number of defects through the reactions

$$C_x + C_y \rightarrow C_z , \qquad (30a)$$

$$C_x + C_z \rightarrow C_y , \qquad (30b)$$

$$C_y + C_z \rightarrow C_x . \qquad (30c)$$

Reactions (30a) and (30b) were observed frequently in the simulation; the inverse reactions $C_z \rightarrow C_x + C_y$ and $C_y \rightarrow C_x + C_z$ were observed only occasionally, and were always followed by the annihilation of the generated C_x defect, through reactions (30b), (30a), or the inverse of the reaction (30c), i.e., $C_x \rightarrow C_y + C_z$. This leads us to conclude that the reactions $C_x + C_y \rightarrow C_z$ and $C_x + C_z \rightarrow C_y$ are exoergic, while the reaction $C_y + C_z \rightarrow C_x$ is endoergic. The system therefore tends to annihilate the C_x defect whenever another defect is found in its vicinity, while the production of the C_x defect is always energetically disadvantageous, which explains the rapid annihilation of the C_x population. It is interesting to note that the C_x defects appear in the system in small numbers even at very late times (see Table II); the apparent reason is that a C_y or C_z defect can use a short-lived creation of the C_x defect to move through the system [see Figs. 18(c)–18(e)] in order to take part in the $C_y + C_y \rightarrow C_0$ and $C_z + C_z \rightarrow C_0$ reactions, which are the dominant decay channels in the late time regime.

No decay channel in which the number of C_y defects is reduced without producing a C_z defect (or vice versa) is available, except for the mutual annihilation of two C_y or C_z defects; these occur with a probability proportional to the square of the number density of the C_y or C_z species, which remain approximately equal, because the two species were present at roughly equal numbers when

the C_x defects disappeared from the system. The numbers of C_y and C_z defects are thus locked at late times; the explanation of the slight difference in the effective exponents describing their decay with time would require a more detailed knowledge of the energetics of the processes involved, including the reactions involving the catalyst C_x. Thus far, we have not included in our discussion the influence of the $\overline{C}_0$ ($360°$) defects. These were present only in small numbers, even at the later times, when the $\overline{C}_0$ defect-counting algorithm overcomes the problem discussed earlier in this section. It is also clear from Table I that the events involving the $\overline{C}_0$ defects cannot change the mechanism of the C_y and C_z species selection, discussed above. The tendency of the $\overline{C}_0$ defect population to decay at a rate similar to the decay rate of the C_y and C_z defect populations at late times is readily understood: the process $\overline{C}_0 + \overline{C}_0 \rightarrow C_0$ has a low probability, because the number density of the $\overline{C}_0$ defects is very low. Instead, the decay channels $\overline{C}_0 + C_y \rightarrow C_y$ and $\overline{C}_0 + C_z \rightarrow C_z$, occurring at rates tied to the number densities of the C_y and C_z defects, will prevail.

We end by noting that the main points of the discussion of the $\{C_x, C_y, C_z\}$ system presented in this section should be relevant to any three- (or more-) component system exhibiting "cyclic" reactions such as (30a)–(30c).

VI. SUMMARY AND CONCLUSIONS

Detailed analysis of our results showed that dynamical scaling is violated throughout the studied time range. To reach this conclusion, we had to compare the growth laws for the correlation length and for the average separation between topological defects. Studying the correlation function alone does not indicate the violation of dynamical scaling. We also showed that the observed discrepancy between the growth exponents of the correlation length and of the characteristic length determined from the energy density does not necessarily indicate a violation of dynamical scaling.

In order to explain why the growth exponents observed in our simulations were significantly lower than 0.5, we studied the annihilation process of an isolated pair of uniaxial nematic defects. Our results show that the lowered value of the effective growth exponent ϕ_{def} for the average separation of defects may be understood by analyzing the forces acting on the point defects, similarly to the treatment of phase ordering in the $O(2)$ vector model in [17].

The analysis discussed in the preceding paragraph suggests that the effective growth exponent ϕ_{def} should approach the value of 0.5 in the regime where the average separation between defects becomes much larger than the size of the defect cores. In this regime we expect that the growth exponent for the correlation length, ϕ_{cor}, also reaches the value of 0.5, and the correlation function truly collapses. The difference between ϕ_{cor} and the growth exponent for the energy length (ϕ_{en}), analyzed in Sec. III D, is predicted to vanish in this regime [see Eq. (23)]. We therefore expect that in the late stages of the phase or-

dering of a sufficiently large nematic system, dynamical scaling will hold, and that all characteristic length scales in the system will grow as a power law of time with the growth exponent equal to 0.5. Due to the logarithmic corrections to the true asymptotic values of the growth exponents, studied in Secs. III D and V A, however, it is not presently possible to access the true scaling regime in computer simulations.

An important ingredient missing from the analysis of the behavior of the growth exponents is an explanation of the discrepancy between the growth exponents for the average separation of defects and for the correlation length. An analytical and numerical analysis of the role of degrees of freedom other than the defect coordinates in the phase ordering process is currently in progress [18].

In Secs. IV and V B, we studied the properties of the four topologically distinct species of defects present in a biaxial nematic system during the phase ordering process. The topological character of the defects and the defect interactions observed in our simulations agree with the predictions of the topological classification scheme. Of the four allowed defect species, only two were observed in large numbers at late stages of the ordering process. We proposed a mechanism for the selection of the prevailing defect species, based on the combination laws following from the topological classification scheme.

It would be interesting to test these predictions experimentally.

Note added in proof. We recently learned of the work of C. Kobdaj and S. Thomas [Nucl. Phys. **B413**, 689 (1994)], which investigates the energies and interaction potentials of non-Abelian defects in two dimensions that are topologically equivalent to the biaxial nematic defects investigated in Secs. IV and V B of the present paper. Kobdaj and Thomas show that the C_x defect (corresponding to the C_k defect in their notation) is energetically unstable towards the dissociation into a C_y defect plus a C_z defect. This directly explains the rapid decay of the C_x population observed in our phase ordering simulation, and confirms the mechanism of the selection of defect species proposed in Sec. V B.

ACKNOWLEDGMENTS

[1] For a review see, e.g., J. D. Gunton, M. San Miguel, and P. S. Sahni, in *Phase Transitions and Critical Phenomena*, edited by C. Domb and J. L. Lebowitz (Academic Press, New York, 1983), Vol. 8.
[2] Recent results in phase ordering of systems with continuous symmetry are reviewed in A. J. Bray, Physica A **194**, 41 (1993).
[3] M. Mondello and N. Goldenfeld, Phys. Rev. A **42**, 5865 (1990).
[4] M. Mondello and N. Goldenfeld, Phys. Rev. A **45**, 657 (1992).
[5] I. Chuang, R. Durrer, N. Turok, and B. Yurke, Science **251**, 1336 (1991).
[6] I. Chuang, B. Yurke, A. N. Pargelis, and N. Turok, Phys. Rev. E **47**, 3343 (1993).
[7] A. P. Y. Wong, P. Wiltzius, and B. Yurke, Phys. Rev. Lett. **69**, 3583 (1992); A. P. Y. Wong, P. Wiltzius, R. G. Larson, and B. Yurke, Phys. Rev. E **47**, 2683 (1993).
[8] R. E. Blundell and A. J. Bray, Phys. Rev. A **46**, 6154 (1992).
[9] H. Toyoki, Phys. Rev. E **47**, 2558 (1993).
[10] A. J. Bray, S. Puri, R. E. Blundell, and A. M. Somoza, Phys. Rev. E **47**, 2261 (1993).
[11] Y. Oono and S. Puri, Phys. Rev. Lett. **58**, 836 (1987); Phys. Rev. A **38**, 434 (1988).
[12] A. J. Bray and A. D. Rutenberg, Phys. Rev. E **49**, 27 (1994).
[13] T. Ohta, D. Jasnow, and K. Kawasaki, Phys. Rev. Lett. **49**, 1223 (1982).
[14] R. E. Blundell and A. J. Bray, Phys. Rev. E **49**, 4925 (1994).
[15] N. D. Mermin, Rev. Mod. Phys. **51**, 591 (1979).
[16] I. M. Lifschitz, Zh. Eksp. Teor. Fiz. **42**, 1354 (1962) [Sov. Phys. JETP **15**, 939 (1962)]; S. M. Allen and J. W. Cahn, Acta Metall. **27**, 1085 (1979).
[17] B. Yurke, A. N. Pargelis, T. Kovacs, and D. A. Huse, Phys. Rev. E **47**, 1525 (1993).
[18] M. Zapotocky, P. M. Goldbart, and N. Goldenfeld (unpublished).
[19] See, e.g., P.-G. de Gennes, *The Physics of Liquid Crystals* (Clarendon, Oxford, 1974).
[20] Note that the order parameter tensor $Q_{\alpha\beta}$ can be expressed in terms of the components of the uniaxial axis $\pm\mathbf{u}$ and biaxial axis $\pm\mathbf{b}$ as $Q_{\alpha\beta} = \frac{3}{2}S_1(u_\alpha u_\beta - \frac{1}{3}\delta_{\alpha\beta}) + \frac{1}{2}S_2(b_\alpha b_\beta - v_\alpha v_\beta)$, where $\mathbf{v} = \mathbf{u} \times \mathbf{b}$. The scalars S_1 (S_2) determine the strength of uniaxial (biaxial) ordering.
[21] E. Gramsbergen, L. Longa, and W. de Jeu, Phys. Rep. **135**, 196 (1986).
[22] A. J. Bray and K. Humayun, Phys. Rev. E **47**, 9 (1993).
[23] H. Toyoki, Phys. Rev. B **45**, 1965 (1992).
[24] Although we find that the correlation length and the separation of defects have slightly different growth exponents (see Sec. V A), over the range of times accessible in our simulation they remain comparable in magnitude.
[25] See, however, the discussion of the contrary case in Sec. V A. In fact, Porod's law in the form $S(k,t) = A\rho_{\rm def}(t)k^{-\chi}$ is valid independently of any scaling assumptions. The exponent χ and the amplitude A were calculated exactly (from the order parameter configuration of an isolated defect) in Ref. [22] for the $O(N)$ vector model case. Analogous calculations have been performed for the uniaxial and biaxial nematic cases, and will be reported in a separate presentation.
[26] This is, of course, only valid provided topological defects can exist in the system. An example of a system where no singular topologically stable objects can exist is the

O(N) vector model in d dimensions for $N > d$ (see, e.g., Ref. [15]).

[27] In three spatial dimensions, there is another consequence of the noncommutative character of the first homotopy group: some of the line defects classified by Π_1 cannot cross due to topological obstructions [see V. Poénaru and G. Toulouse, J. Phys. (Paris) **8**, 887 (1977)]. One may expect this to lead to a slowing down or complete impairment of the phase ordering process in three-dimensional biaxial nematic systems [18].

[28] T. De'Neve, M. Kleman, and P. Navard, J. Phys. II (France) **2**, 187 (1992).

[29] Note that in the uniaxial quench case, intersections of four dark brushes (occasionally appearing in our Schlieren pictures) should not be interpreted as a topological defect. For example, the topologically trivial configuration in Fig. 12(a), and the configurations generated during the escape of such a configuration to the uniform configuration in Fig. 12(b), would appear as such an intersection.

[30] A. J. Bray, S. Puri, and K. Humayun (unpublished); M. Zapotocky and W. J. Zakrzewski (unpublished).
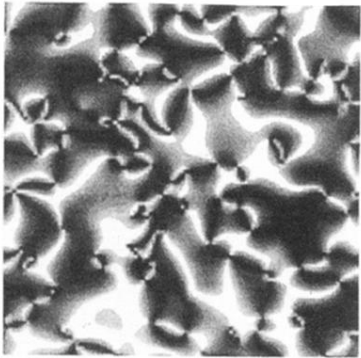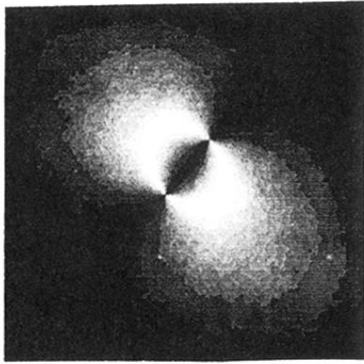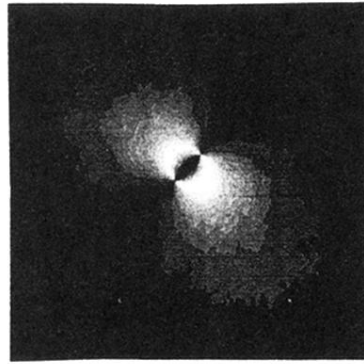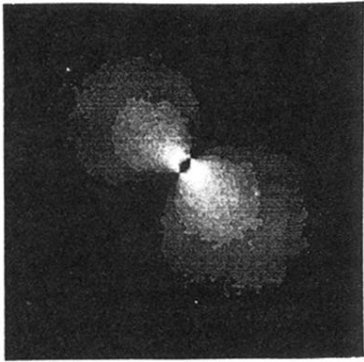
a) $t = 500$
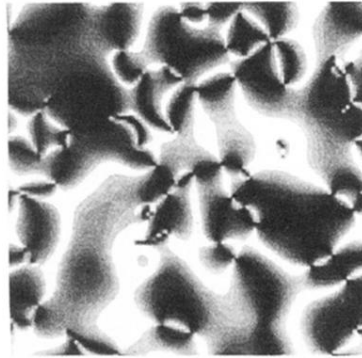
b) $t = 1000$
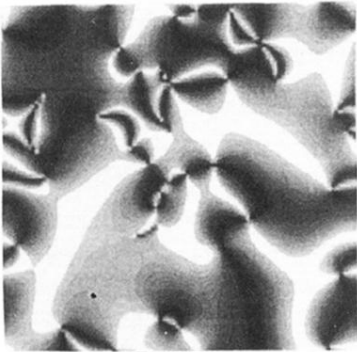
c) $t = 2000$

FIG. 17. Intensity of light transmitted through a uniaxial nematic film situated between crossed polarizers (the Schlieren pattern). We show a system of size 100×100 at times $t = 500$, $t = 1000$, and $t = 2000$ after the quench. The defects appear in the pictures as the intersections of two bright and two dark lines.
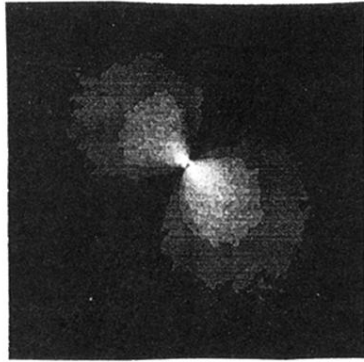
a) $\tau = 3265$

b) $\tau = 465$

c) $\tau = 30$

d) $\tau = 0$

FIG. 20. Schlieren patterns showing two approaching uniaxial defects at times $t=3265$, $t=465$, and $t=30$ before annihilation, and one time step after annihilation. The system size was 100×100; the value of the diffusion constant was $D = 0.3$; weak noise (10% of the order parameter magnitude) was added at each time step.